الجمهورية الجزائرية الديمقراطية الشعبية
REPUBLIQUE ALGERIENNE DEMOCRATIQUE ET POPULAIRE
وزارة التعليم العالي و البحث العلمي
Ministère de l'Enseignement Supérieur et de la Recherche Scientifique
جامعة أبي بكر بلقايد – تلمسان –
Université Aboubakr Belkaïd – Tlemcen –
Faculté de TECHNOLOGIE

MEMOIRE

Présenté pour l'obtention du **diplôme** de **MASTER**

En : Télécommunications

Spécialité : Réseaux et Télécommunications

Par : MELLOUK Amira Othmania et BENYOUB Romayssa Chaima

Sujet

Visible Light Communication (VLC)-Based Vehicle Positioning Using Optical Retroreflection

Soutenu publiquement, le 18/06/2026, devant le jury composé de :

BAHRI SIDI MOHAMMED	MCA	Université de Tlemcen	Président
KHELLADI Mounir	MCA	Université de Tlemcen	Examinateur
BOUACHA Abdelhafid	Professeur	Université de Tlemcen	Encadrant

Année universitaire : 2025/2026

Dedication

To the soul of my beloved **Grandmother,**

You left before you could see this moment, but I felt your presence in every step.
Your gentleness, your duas, and the warmth of your hands
have never truly left me.
I carry you in my heart always may Allah grant you His mercy and the highest place in Jannah.
رحمك الله يا جدتي

To my beloved Mother and Father,

You are the roots that held me steady and the wings that let me rise.
Every page of this work carries a breath of your patience, your prayers,
and the endless love you have poured into my life without ever asking for anything in return.
No words are enough this is yours before it is mine.

To my twin **Amir,**

We came into this world together, and I have never once felt alone because of that.
You are my mirror, my rival, and my closest friend.
May this work remind you that everything we dream is within reach.

And to my little sister **Meriam,**

Your laughter has always been the lightest thing in any room.
Grow boldly the world is wide and you are more than ready for it.

To my brother **Zakaria**, *his wife* **Selma**, *and their little ones* **Lyna** *and* **Chakib,**

Thank you for building a home full of warmth and welcome,
and for showing me what it means to carry a family with grace and strength.
Lyna and Chakib you make every return home feel like the best part of any journey.

To my brother **Imad**, *his wife* **Ahlem**, *and their little sunshine* **Nouha,**

Your quiet support and steady presence have meant more than you know.
Thank you for always believing in me, even in moments I doubted myself.
Nouha may you always look at the world with those bright, wondering eyes.

To my dear **Aunt,** *who recently joined our little family after the passing of my grandmother*

To my teammate and partner in this journey, **Romayssa,**

What began as a shared project became a shared success.
Thank you for your dedication, your patience through every obstacle,
and for always showing up — even on the hardest days.
This work belongs to both of us equally.

Amira,

Dedication

I dedicate this work, with all my love and deepest gratitude, to every soul who made me who I am today.

To my mother, Djamila,

You are my safe haven, my compass, and my greatest strength.
On the days I stopped believing in myself, you never did.
Your love is the foundation of everything I have ever built.
This work belongs to you more than it belongs to me.

To my father, Noureddine,

You taught me that dignity lives in hard work, and pride lives in silence.
Your sacrifices never asked for recognition; they simply shaped me.
I carry your values in everything I do, and I am endlessly proud to be your daughter.

To my sister Hassna, her husband Samir, and their little ones Mila and Kinane,

Your home has always been my shelter, your warmth my comfort,
and your presence a reminder that I am never truly alone.
Thank you for loving me the way you do quietly, steadily.
Mila and Kinane you make every moment brighter just by being in it.
You are the sweetest chapter in our family's story.

To my brothers, Kader, Hamza, and Yasser,

You are my pride, my anchor, and my reason to always give my best.
I carry your names with honor in everything I do,
and I hope one day this work makes you proud.

To my teammate and friend, Amira,

You walked every step of this journey beside me
through the doubt, exhaustion , and all the moments we almost gave up.
This work carries your fingerprints too.

And last but not least to myself,

I want to thank myself for believing in me,
for having no days off, for never quitting,
and for never giving up even when it was the easiest option.
I am proud of me.

ROMAYSSA

Abstract

This thesis proposes a Visible Light Communication (VLC)-based positioning system for urban vehicles, exploiting optical retroreflection to overcome the limitations of Global Navigation Satellite Systems (GNSS) in dense urban canyons. The system leverages existing retroreflective elements on road vehicles—such as bumper reflectors and license plate housings—as passive optical landmarks, thereby eliminating the need for an active transmitter on the target vehicle. A monostatic Angle Diversity Receiver (ADR) onboard the transmitting vehicle captures the retroreflected echo, enabling simultaneous ranging and channel estimation from a single LED signal.

A comprehensive mathematical framework is developed, combining a Lambertian propagation model with a Corner-Cube Retroreflector (CCR) gain function to yield a $1/d^4$ round-trip channel law. The vehicle's position is estimated by formulating a weighted nonlinear least-squares problem solved via the Levenberg–Marquardt algorithm. The resulting estimates directly feed a Zero-Forcing (ZF) precoder without introducing pilot overhead. Monte Carlo simulations demonstrate sub-decimeter longitudinal accuracy at ranges up to 30 m under nighttime conditions and 10 to 15 m during daytime conditions. These results confirm that the proposed system offers a low-cost, scalable, and GNSS-complementary solution for next-generation Intelligent Transportation Systems (ITS).

Keywords— VLC, vehicle positioning, retroreflection, CCR, ADR, Levenberg–Marquardt, channel estimation, ITS.

Résumé

Cette thèse propose un système de positionnement de véhicules urbains basé sur la Communication par Lumière Visible (VLC) et la rétroréflexion optique, afin de pallier les limites du GNSS en milieu urbain dense. Le système exploite les réflecteurs déjà présents sur les véhicules comme repères optiques passifs, capturés par un récepteur à diversité angulaire (ADR) monostatique permettant d'estimer simultanément la position et le canal optique à partir d'un signal LED unique, grâce à l'algorithme de Levenberg–Marquardt. Les simulations de Monte Carlo montrent une précision longitudinale sous-décimétrique jusqu'à 30 m de nuit, et de 10 à 15 m de jour, confirmant l'intérêt de cette solution économique et complémentaire au GNSS pour les systèmes de transport intelligents (ITS) de nouvelle génération.

Mots-clés— *VLC, positionnement de véhicules, rétroréflexion, CCR, ADR, algorithme de Levenberg–Marquardt, estimation de canal, ITS.*

ملخص

تقترح هذه الأطروحة نظاماً لتحديد موقع المركبات يستند إلى تقنية الاتصال بالضوء المرئي (VLC) والانعكاس الضوئي الرجعي لتجاوز إخفاقات GNSS في الأنفاق الحضرية. يستغل النظام العناصر العاكسة للضوء الموجودة بالفعل على المركبات — كعواكس المصدات ولوحات الترخيص — بوصفها معالم ضوئية سلبية، ملغياً الحاجة إلى أي مرسل نشط على المركبة المستهدفة. يعتمد النظام على جهاز استقبال تنوع زاوية (ADR) أحادي المركز لالتقاط صدى الانعكاس وتقدير المسافة والقناة في آن، بإطار رياضي يجمع نموذج لامبيرتي وكفاءة عاكس الزاوية (CCR) لينتج قانون تخفّف $1/d^4$. يُحل مشكلة تحديد الموقع بوصفها تحسيناً للمربعات الصغرى غير الخطية الموزونة عبر خوارزمية ليفنبرغ–ماركواردت، وتُغذّي نتائجها مباشرةً مشفّر إلغاء التدخل (ZF) دون رموز تدريبية. تتحقّق محاكاة مونتي كارلو دقة طولية دون عشرة سنتيمترات حتى 30 متراً ليلاً، وتصل إلى 15 متراً نهاراً، مقدّماً حلاً متكاملاً مع GNSS لأنظمة النقل الذكي.

الكلمات المفتاحية : *VLC، تحديد موقع المركبات، انعكاس ضوئي رجعي، ADR، CCR، خوارزمية LM، تقدير القناة، ITS.*

Acknowledgments

F irst and foremost, we give all praise and gratitude to God Almighty, whose grace, mercy, and blessings guided our steps throughout this journey. It is by His will that this work came to fruition, and it is to Him that we owe every success, every moment of clarity, and every ounce of perseverance that carried us through the most difficult stages of this research.

We would then like to express our deepest and most sincere gratitude to our thesis supervisor, **Mr. BOUACHA**, for his constant guidance, availability, and expert advice throughout the entire duration of this work. His rigorous supervision, constructive feedback, and genuine commitment to our progress were fundamental in shaping the direction and academic quality of this research. We are truly grateful for the trust he placed in us and for the time and effort he devoted to our academic development.

We wish to extend our heartfelt thanks to the internship supervisors, **Mr. OUCHIKH** and **Mr. MOHAMMEDI**, for welcoming us and for the valuable professional experience they provided during our internship period. Their practical insight, patience, and willingness to share their knowledge played a decisive role in our understanding of real-world applications of the concepts studied in this thesis. Their support and mentorship went well beyond what was required, and for that we are sincerely grateful.

We are also grateful to the members of the thesis examination committee for agreeing to evaluate this work and for their time and expertise. Their remarks and questions will undoubtedly contribute to deepening the reflections initiated by this research.

Our sincere thanks go as well to all the faculty members and teaching staff who contributed to our academic training throughout our years of study. The knowledge, scientific rigor, and intellectual curiosity they instilled in us formed the solid foundation upon which this research was built.

This work would not have been possible without the support of our colleagues and fellow students, whose stimulating discussions, shared curiosity, and encouragement created a truly collaborative and enriching research environment. We are thankful for every exchange that helped us see the problem from a different angle.

On a personal note, we owe an immeasurable debt of gratitude to our family, whose unconditional love, sacrifice, and moral support sustained us throughout the long and demanding process of completing this thesis. Their belief in us never wavered, and their patience and encouragement were our greatest source of strength.

Finally, we would like to acknowledge all those who, in one way or another, contributed to the completion of this work — whether through a word of advice, a moment of support, or simply by being present. Every contribution, however small, has left its mark on these pages.

"Science is not a solitary pursuit — it is built on the shoulders of those who came before, and sustained by those who walk beside us."

List of Abbreviations

Abbreviation	Full Term
ADAS	Advanced Driver Assistance Systems
AOA	Angle of Arrival
APD	Avalanche Photodiode
ATMS	Advanced Traffic Management Systems
BeiDou	Chinese Navigation Satellite System
C-ACC	Cooperative Adaptive Cruise Control
CAV	Connected and Autonomous Vehicle
CIR	Channel Impulse Response
C-V2X	Cellular Vehicle-to-Everything
DCO-OFDM	DC-biased Optical OFDM
ACO-OFDM	Asymmetrically Clipped Optical OFDM
DGNSS	Differential Global Navigation Satellite System
DOP	Dilution of Precision
DSRC	Dedicated Short Range Communications
GDOP	Geometric Dilution of Precision
Galileo	European Global Navigation Satellite System
GLONASS	Global Navigation Satellite System (Russian)
GNSS	Global Navigation Satellite System
GPS	Global Positioning System
IM/DD	Intensity Modulation / Direct Detection
INS	Inertial Navigation System
IoT	Internet of Things
ITS	Intelligent Transportation Systems
LED	Light Emitting Diode
LiDAR	Light Detection and Ranging
LMS	Least Mean Squares
LoS	Line-of-Sight
LS	Least Squares
MMSE	Minimum Mean Square Error
NLOS	Non-Line-of-Sight

(continued on next page)

(continued from previous page)

Abbreviation	Full Term
OFDM	Orthogonal Frequency Division Multiplexing
OOK	On-Off Keying
PAM	Pulse Amplitude Modulation
PD	Photodiode
PIN	Positive-Intrinsic-Negative (photodiode)
PPM	Pulse Position Modulation
RF	Radio Frequency
RLS	Recursive Least Squares
RMS	Root Mean Square
RSS	Received Signal Strength
RTK	Real-Time Kinematic
SAE	Society of Automotive Engineers
SLAM	Simultaneous Localization and Mapping
SNR	Signal-to-Noise Ratio
TDOA	Time Difference of Arrival
TOA	Time of Arrival
UWB	Ultra-Wideband
V2I	Vehicle-to-Infrastructure
V2V	Vehicle-to-Vehicle
V2X	Vehicle-to-Everything
VLC	Visible Light Communication

Contents

Abstract iii

Acknowledgments v

List of Abbreviations vii

Introduction 2

1 Background and Problem Statement 6

1.1 Introduction . . . 6
1.2 Vehicle Positioning in Intelligent Transportation Systems . . . 6
1.2.1 Global Navigation Satellite Systems and Their Urban Limitations . . . 7
1.2.2 Complementary Positioning Technologies . . . 7
1.3 Fundamentals of Visible Light Communication . . . 8
1.3.1 General principles of VLC . . . 8
1.3.2 VLC for Vehicle-to-Infrastructure (V2I) Communication . . . 9
1.3.3 Specific Constraints of Outdoor VLC . . . 9
1.4 VLC-Based Positioning Techniques . . . 10
1.4.1 Received Signal Strength (RSS) Positioning . . . 10
1.4.2 Time-Based Positioning: TOA and TDOA . . . 11
1.4.3 Angle of Arrival (AOA) Positioning . . . 11
1.4.4 Limitations in Dynamic Urban Environments . . . 11
1.5 Optical Retroreflection . . . 12
1.5.1 Physical Principles and Mathematical Modeling . . . 12
1.5.2 Existing Applications in Transportation . . . 13
1.5.3 Interest for Passive Low-Complexity VLC Positioning . . . 14
1.6 VLC Channel Estimation and Its Link to Localization . . . 14
1.6.1 Optical Propagation Models in Urban Environments . . . 15
1.6.2 Channel Estimation Techniques in VLC . . . 15
1.6.3 Channel Parameters as Sources of Position Information . . . 16
1.7 Critical Review of the State of the Art . . . 17
1.8 Conclusion . . . 18

2 System Modeling and VLC-Based Positioning Method **21**
2.1 Introduction . . . 21
2.2 Architecture of the Proposed Vehicular VLC System . . . 21
2.2.1 System Overview . . . 21
2.2.2 LED Transmitter Assembly . . . 22
2.2.3 Angle Diversity Receiver (ADR) . . . 23
2.2.4 Passive Retroreflective Element (CCR) . . . 23
2.3 VLC Channel Modeling with Retroreflection . . . 25
2.3.1 Lambertian Line-of-Sight Forward Model . . . 25
2.3.2 Corner-Cube Retroreflector (CCR) Model . . . 25
2.3.3 Retroreflected Channel Gain . . . 26
2.3.4 Communication Channel at Vehicle B . . . 27
2.3.5 Noise Modeling . . . 27
2.4 Signal Model and Channel Estimation at the ADR . . . 29
2.4.1 ADR Signal Measurement Vector . . . 29
2.4.2 Compound Parabolic Concentrator (CPC) Design . . . 29
2.4.3 Sensitivity Analysis: Distance and Angular Effects . . . 31
2.4.4 Robustness to Ambient Perturbations . . . 31
2.5 Positioning Method Based on Channel Estimation . . . 32
2.5.1 Mathematical Formulation of the Positioning Problem . . . 32
2.5.2 Levenberg–Marquardt Algorithm . . . 32
2.5.3 Initialization Strategy . . . 33
2.5.4 Channel Estimation from Positioning . . . 34
2.5.5 Zero-Forcing Precoding Based on Estimated CSI . . . 34
2.5.6 Generalization to Multiple CCRs . . . 35
2.6 Conclusion . . . 35

3 Simulation Results and Performance Evaluation **38**
3.1 Introduction . . . 38
3.2 Simulation Parameters . . . 38
3.3 Description of the VLC Simulation Interface . . . 40
3.4 General Scenario Overview . . . 41
3.5 Case 1: Aligned Configuration . . . 42
3.5.1 SNR versus Distance . . . 43
3.5.2 CDF of Measurement Error . . . 45
3.5.3 Coverage Probability $P(\geq 2$ PDs) vs. Overlap Factor . . . 46
3.5.4 CDF of Positioning Error . . . 47
3.5.5 CDF of Sum Spectral Efficiency . . . 48

3.6 Case 2 : Lateral Offset Configuration ($d_y \neq 0$) 49
3.6.1 Sub-config A: $d_x = 15$ m, $d_y = 2$ m, $N = 5$, $O_v = 0.5$ 49
3.6.2 Sub-config B: $d_x = 10.5$ m, $d_y = 6.5$ m, $N = 2$ 54
3.7 Ideal Case: Noise-Free Bound 59
3.8 Discussion and Performance Synthesis 60
3.8.1 Geometric Constraints and Spatial Availability 60
3.8.2 Noise Sensitivity and Ambient Light Degradation 61
3.8.3 Downstream Impact on Positioning and Throughput 61
3.8.4 Key Design Recommendations 61
3.9 Conclusion 62

General Conclusion **64**

List of Figures

1.1 Comparison of positioning technologies for urban ITS applications 8
1.2 Generic VLC-based V2I communication architecture for urban environments. 10
1.3 Physical principles of optical retroreflection and the monostatic vehicular VLC link model. 13
1.4 Channel estimation pipeline for VLC-based localization 16

2.1 Complete architecture of the proposed retroreflective V2V VLC positioning system. 22
2.2 Exemple of modern automotive front-lighting LEDs. 23
2.3 Diagram of the ADR system and retro-reflection-based VLC positioning principle. 24
2.4 Geometric Analysis and Automotive Integration of a Corner-Cube Retroreflector (CCR) for Passive VLC Positioning. 24
2.5 ADR geometric configuration showing CPC-coupled photodiodes and their angular orientations 30
2.6 Multi-CCR generalization of a retroreflection VLC positioning. 36

3.1 Screenshot of the *VLC Positioning Simulator*. 41

3.2 Top-view scene: $d_x = 15$ m, $d_y = 0$ m, $N = 3$, $O_v = 0$. Green cones: active ADR FoV; grey: inactive. Orange square: true CCR position; red cross: LM estimate. 43
3.3 Mean SNR versus longitudinal distance d_x. Configuration: $d_x = 15$ m, $d_y = 0$ m, and $N = 3$. Comparison between overlap configurations $O_v = 0$ and $O_v = 1$ under daytime and night-time conditions. 44
3.4 CDF of measurement error: $d_x = 15$ m, $d_y = 0$, $N = 3$, $O_v = 0$. Daytime and night-time conditions. 45
3.5 $P(\geq 2$ PDs receiving) vs. overlap factor O_v. Configuration: $d_x = 15$ m, $d_y = 0$, $N = 3$. $N = 2, 3, 4, 5$ compared. $N_{\text{trials}} = 2000$. 46

3.6 CDF of Euclidean positioning error Δu. Configuration: $d_x = 15$ m, $d_y = 0$, $O_v = 0$. $N = 3$ and $N = 5$, daytime and night-time. $N_{\text{mc}} = 400$. 47
3.7 CDF of SSE: $d_x = 8$ m, $d_y = 0$, $O_v = 0$. Black: ideal. Coloured: position-based estimation. Night-time. 48
3.8 Top-view scene: $d_x = 15$ m, $d_y = 2$ m, $N = 5$, $O_v = 0.5$. Enhanced ADR configuration improves FoV coverage for moderate lateral offset. 49
3.9 Mean SNR vs. longitudinal distance d_x. Configuration: $d_x = 15$ m, $d_y = 0$ m, $N = 4$, $O_v = 0$. Night-time (solid blue) and daytime (dashed orange) conditions. Marked operating point at $d_x = 15$ m: night 10.8 dB, day −2.7 dB. 50
3.10 CDF of positioning error Δu: $d_x = 15$ m, $d_y = 2$ m, $N = 5$, $O_v = 0.5$. Night-time median: 1.10 m; daytime median: 1.04 m. $N_{\text{mc}} = 400$ Monte Carlo trials. 51
3.11 $P(\geq 2$ PDs receiving) vs. O_v. Sub-config A: $d_y = 2$ m, $N = 5$, $O_v = 0.5$. $N = 2, 3, 4, 5$ compared. 52
3.12 CDF of positioning error Δu: $d_x = 15$ m, $d_y = 2$ m, $N = 5$, $O_v = 0.5$. Daytime and night-time. $N_{\text{mc}} = 400$. 53
3.13 CDF of SSE for $d_x = 15$ m, $d_y = 2$ m, $N \in 3, 5$ and $O_v = 0.5$. 54
3.14 Top-view scene for $d_x = 10.5$ m, $d_y = 6.5$ m, $N = 2$, and $O_v = 0$. 55
3.15 Average SNR versus longitudinal distance (d_x) for ($d_y = 6.5$) m, ($N = 2$), and ($O_v = 0$) under day-time and night-time conditions. 56
3.16 CDF of measurement error (d_x) for $d_y = 6.5$ m, $N = 2$, and $O_v = 0$ under daytime and night-time conditions. 56
3.17 Coverage probability $P(\geq 2$ PDs receiving) vs. overlapping factor O_v for $d_y = 6.5$ m, comparing array densities $N = 2, 3, 4$, and 5. 57
3.18 CDF of positioning error (Euclidean distance) for $d_x = 10$ m and $d_y = 6.5$ m, comparing $N = 3$ and $N = 5$ under daytime and night-time conditions. . . . 58
3.19 CDF of Sum Spectral Efficiency (SSE) at $d_x = 10$ m and $d_y = 6.5$ m under night-time conditions, comparing the real channel against position-based estimation configurations ($N = 3$ and $N = 5$). 59

List of Tables

1.1 Comparative Overview of VLC-Based Positioning Methods 12
1.2 Comparison of Related Works in VLC and Retroreflective Systems 18

3.1 Simulation parameters. 39
3.2 Performance summary across noise scenarios ($N = 3$, $O_v = 0$, $d_x \in [5, 30]$ m, $d_y = 0$). 60

GENERAL INTRODUCTION

Introduction

The rapid expansion of connected and autonomous vehicles has imposed unprecedented demands on positioning technology. Modern Intelligent Transportation Systems (ITS) require centimeter- to lane-level accuracy to support safety-critical functions such as cooperative adaptive cruise control, automated emergency braking, and intersection management . Conventional satellite-based navigation, encompassing GPS, Galileo, GLONASS, and BeiDou, remains the dominant positioning infrastructure worldwide, achieving meter-level accuracy under open-sky conditions. However, its performance degrades severely in dense urban environments, where satellite signals undergo multipath propagation caused by building facades, bridges, and glass structures, leading to positioning errors that can reach several meters and rendering Global Navigation Satellite Systems (GNSS) incompatible with lane-level applications. Additional vulnerabilities, including complete signal blockage in tunnels and underground areas, and susceptibility to spoofing and jamming attacks, further undermine the reliability of GNSS in urban Intelligent Transportation Systems deployments.

Several complementary technologies have been proposed to bridge this gap. Inertial Navigation Systems (INS) provide short-term continuity during GNSS outages but accumulate unbounded drift over time due to sensor errors. LiDAR-based localization achieves high precision through point-cloud matching against pre-built maps, yet carries prohibitive hardware cost, heavy computational overhead, and significant performance degradation in adverse weather conditions such as fog, rain, and snow. Radio-based techniques exploiting Time of Arrival (TOA), Time Difference of Arrival (TDOA), Angle of Arrival (AOA), or Received Signal Strength (RSS) from roadside infrastructure improve urban robustness, but remain susceptible to multipath propagation at radio frequencies. Cooperative localization, in which nearby vehicles share positional measurements and fuse them through estimation algorithms, further improves robustness, but demands reliable inter-vehicle communication links that are themselves difficult to guarantee in dense traffic.

In this context, Visible Light Communication (VLC) has emerged as a fundamentally different and attractive alternative for urban vehicular positioning. VLC exploits the visible light spectrum, ranging from approximately 400 nm to 700 nm, to transmit data using the intensity modulation of LED sources, allowing the same fixture that provides road illumination to simultaneously serve as a localization beacon. Because light does not penetrate opaque obstacles, VLC eliminates large-scale multipath and is inherently immune to electromagnetic interference. The visible spectrum offers bandwidth several thousand times larger than the entire radio-frequency spectrum, and the reuse of existing LED infrastructure, traffic lights,

street lamps, and road signs, drastically reduces deployment cost compared to dedicated radio base stations. These properties make VLC an attractive complement to GNSS in exactly the urban canyon environments where satellite navigation is most degraded.

Despite these advantages, the overwhelming majority of existing VLC-based positioning systems share a critical architectural limitation: they require active optical transmitters on both ends of the communication link. This bilateral architecture increases deployment cost, introduces clock synchronization complexity between spatially separated nodes, and raises maintenance requirements on roadside infrastructure. These barriers have prevented the practical adoption of VLC positioning in real vehicular environments, motivating the search for a simpler and more scalable solution.

Optical retroreflection offers a compelling path forward. A retroreflector is a passive optical element that returns incident light almost exactly toward its source, regardless of surface orientation, within a defined angular acceptance range. Corner-cube retroreflectors (CCRs), already embedded in automotive tail reflectors, traffic signs, and lane markings, can serve as passive positioning landmarks requiring no electrical supply, no synchronization circuitry, and no communication module. A vehicle equipped with LED headlights and an Angle Diversity Receiver (ADR), forming a monostatic transceiver, can emit a modulated optical signal, capture the retroreflected echo from the vehicle ahead, and estimate its relative distance and bearing from the round-trip signal power. The combined round-trip power follows a $(1/d^4)$ decay law, analogous to a radar range equation, enabling range estimation from received power without external synchronization . Retroreflective materials are already ubiquitous in road environments, meaning that the proposed system exploits existing passive infrastructure at no additional deployment cost.

This work addresses the design, modeling, and performance evaluation of a retroreflective VLC system for passive vehicle-to-vehicle (V2V) positioning. The proposed architecture places a J-LED headlight array alongside an Angle Diversity Receiver (ADR), consisting of N photodiodes oriented in distinct azimuthal directions, each coupled with a Compound Parabolic Concentrator (CPC), on the transmitting vehicle, while the target vehicle carries only passive corner-cube retroreflectors on its rear surface. The vector of power measurements collected across the ADR encodes both the longitudinal range and the lateral offset to the retroreflector, enabling full two-dimensional localization through a weighted nonlinear least-squares estimator solved by the Levenberg–Marquardt algorithm. The estimated position is then used to reconstruct the direct-link optical channel matrix without pilot symbols or closed-loop feedback, reducing signaling overhead and latency relative to conventional channel estimation approaches. The quality of this position-derived channel estimate is evaluated through its impact on the sum spectral efficiency of a zero-forcing precoder, directly connecting positioning accuracy to communication quality of service.

The remainder of this thesis is organized as follows. Chapter 1 establishes the theoretical

background, covering ITS positioning requirements, the fundamentals of VLC, optical positioning techniques (RSS, TOA, TDOA, AOA), the physics of optical retroreflection, VLC channel estimation methods, and a critical review of the state of the art. Chapter 2 develops the complete system model, encompassing the Lambertian forward channel, the CCR retroreflection model, the ADR signal and noise characterization under outdoor conditions, the CPC optical design, and the full positioning and channel estimation framework. Chapter 3 presents Monte Carlo simulation results evaluating localization error and sum spectral efficiency across a range of operating conditions, including varying inter-vehicle distances, lateral offsets, and daytime versus night-time noise levels. Together, these three chapters constitute a self-contained treatment of a novel passive optical positioning paradigm for urban vehicular environments where GNSS is unreliable.

CHAPITRE

01

BACKGROUND AND PROBLEM STATEMENT



Chapter 1

Background and Problem Statement

1.1 Introduction

The increase of the number of connected vehicles and the push toward autonomous driving have enhanced research in precise vehicle location. Intelligent Transportation Systems (ITS) require positioning methods that surpass conventional satellite navigation. In dense urban environments, satellite signals are frequently blocked or distorted, making accurate lane-level localization difficult to achieve.

Visible Light Communication (VLC) has emerged as a promising complementary technology. It uses existing infrastructure of LED-based traffic lights and street lamps to transmit data and support localization. However, most VLC positioning approaches remain active systems that require powered transmitters on both sides of the link. This increases cost, complexity, and maintenance burden.

This chapter presents the technical background required to understand the proposed approach. It covers the basics of ITS localization, VLC communication, optical positioning techniques, retroreflection, and channel estimation. The chapter concludes with a critical analysis of the state of the art.

1.2 Vehicle Positioning in Intelligent Transportation Systems

Vehicle positioning is one of the core enabling functions in modern ITS. Applications such as lane-level navigation, cooperative adaptive cruise control (C-ACC), intersection management, and automated emergency braking all depend on the ability of a vehicle to determine its location precisely and in real time. As vehicles evolve toward higher levels of automation, the demands on positioning systems increase sharply [1].

According to the U.S. Department of Transportation, cooperative safety applications require sub-meter or lane-level accuracy to function reliably. The European ITS framework similarly identifies precise localization as a prerequisite for advanced driver assistance systems (ADAS) and automated mobility services. Beyond accuracy, ITS positioning systems must satisfy integrity, availability, and continuity requirements [2, 1].

1.2.1 Global Navigation Satellite Systems and Their Urban Limitations

Global Navigation Satellite Systems (GNSS) — including GPS, Galileo, GLONASS, and BeiDou — remain the dominant source of vehicle positioning worldwide. Under open-sky conditions, standard GNSS receivers achieve meter-level accuracy, which is sufficient for many navigation tasks. However, performance degrades severely in dense urban environments [3].

The primary source of degradation in urban areas is multipath propagation. Buildings, bridges, and glass facades reflect satellite signals before they reach the receiver. These reflected signals arrive slightly later than the direct signal, creating erroneous range measurements. The resulting positioning errors can exceed several meters in deep urban canyons, which is entirely incompatible with lane-level applications [3, 4].

A second problem is signal blockage. In tunnels, underground parking lots, and areas with dense tree cover, satellite signals may not reach the receiver at all. When fewer than four satellites are visible, three-dimensional positioning becomes impossible. Even when satellites are available, their geometric configuration, quantified by the Dilution of Precision (DOP) parameter, significantly affects accuracy [4].

A third vulnerability is susceptibility to interference and spoofing. GNSS signals are weak when they arrive at the Earth's surface, making them easy to jam or counterfeit. Spoofing attacks could direct a vehicle to an entirely wrong location, with potentially fatal consequences for autonomous driving [5].

1.2.2 Complementary Positioning Technologies

Augmented GNSS techniques such as Differential GNSS (DGNSS) and Real-Time Kinematic (RTK) positioning improve accuracy to the centimeter level using ground reference stations. However, these systems require stable communication links and depend on satellite visibility, remaining sensitive to multipath [4].

Inertial Navigation Systems (INS) use onboard accelerometers and gyroscopes to estimate vehicle displacement through dead reckoning. INS can maintain positioning continuity during short GNSS outages, but its error grows unboundedly over time due to sensor drift. Without periodic corrections, INS positioning degrades to unusable levels within minutes.

LiDAR-based localization, often combined with Simultaneous Localization and Mapping (SLAM), enables very high precision by matching laser point clouds to pre-built high-definition maps. However, LiDAR systems are expensive, computationally demanding, and sensitive to adverse weather conditions such as rain, fog, and snow.

Communication-based positioning exploits signals from roadside infrastructure using

Time of Arrival (TOA), Time Difference of Arrival (TDOA), Angle of Arrival (AOA), and Received Signal Strength (RSS) techniques. Cooperative localization, in which nearby vehicles share positional measurements, further improves robustness through data fusion [6].

Emerging optical technologies, in particular Visible Light Communication (VLC), offer a fundamentally different propagation medium. Light does not penetrate opaque obstacles, which eliminates large-scale multipath. Combined with existing LED infrastructure, VLC is an attractive option for urban positioning [7, 8].

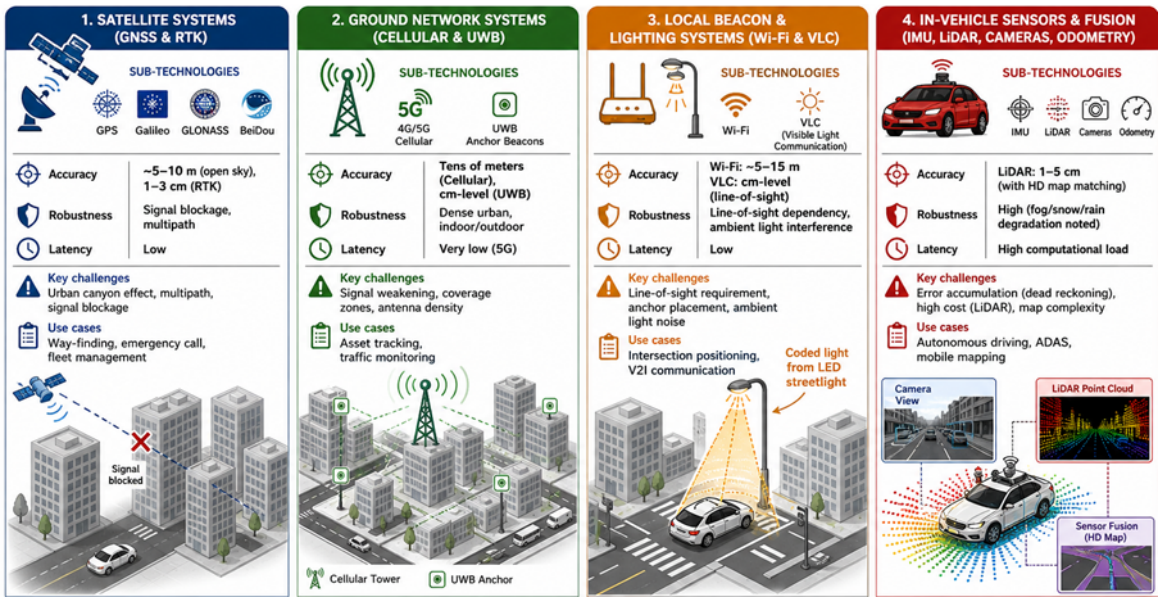


Figure 1.1: *Comparison of positioning technologies for urban ITS applications*

1.3 Fundamentals of Visible Light Communication

1.3.1 General principles of VLC

Visible Light Communication (VLC) is a wireless optical technology that uses the visible light spectrum, ranging from approximately 400 nm to 700 nm, to transmit data. The same LED that provides illumination also acts as a high-speed optical transmitter. Because modern LEDs can be switched at frequencies far beyond human perception, information is encoded in intensity variations the eye never detects [7].

The fundamental building blocks of a VLC system are the LED transmitter, the optical channel, and the photodetector receiver. Because the emitted optical power must always be positive, VLC systems exclusively use Intensity Modulation with Direct Detection (IM/DD). This constrains the applicable modulation schemes to optical-specific techniques [9].

- **On-Off Keying (OOK)**: The simplest scheme, where the LED is either on (‘1’) or off (‘0’). Easy to implement but offers limited spectral efficiency [9].

- **Pulse Position Modulation (PPM)**: Data is encoded in the temporal position of a pulse within a fixed time slot. PPM improves power efficiency but requires accurate timing at the receiver [7].
- **OFDM-based schemes (DCO-OFDM, ACO-OFDM)**: Orthogonal Frequency Division Multiplexing adapted for optical channels. These provide high spectral efficiency and robustness against multipath dispersion [9].

The receiver typically consists of a PIN photodiode or avalanche photodiode (APD), an optical bandpass filter, an amplifier, and a digital signal processor. In outdoor vehicular applications, APDs are preferred for their higher sensitivity. Optical filters suppress ambient light — particularly solar radiation — while passing wavelengths from the intended LED source [10].

1.3.2 VLC for Vehicle-to-Infrastructure (V2I) Communication

Vehicle-to-Infrastructure (V2I) communication using VLC exploits the dense network of LED-based traffic lights, street lamps, and road signs already deployed in modern cities. These elements can serve as both illumination sources and data transmitters, allowing vehicles equipped with photodiode receivers to obtain traffic information and localization references [8].

The key advantages of VLC for V2I scenarios are well-established. The visible light spectrum offers bandwidth several thousand times larger than the entire RF spectrum. VLC produces no electromagnetic interference and provides inherent physical-layer security, since light does not penetrate walls or opaque barriers [7, 11].

Perhaps the most significant practical advantage is infrastructure reuse. Adding VLC capability to an existing LED traffic light requires only a modulation circuit — a minimal cost increment compared to deploying new RF base stations. This drastically reduces deployment barriers [8].

1.3.3 Specific Constraints of Outdoor VLC

Despite its advantages, outdoor vehicular VLC faces several significant challenges. The dominant challenge is solar noise. Sunlight generates a high optical power background that may saturate the photodetector or drown the signal in shot noise. Mitigation strategies include narrow-bandwidth optical filters, adaptive gain control, and narrow field-of-view receiver optics [10].

Atmospheric conditions present another challenge. Fog, rain, and dust scatter light through Mie scattering, increasing channel attenuation and reducing communication range. In dense fog, VLC link distances may drop from tens of meters to just a few meters [10, 12].

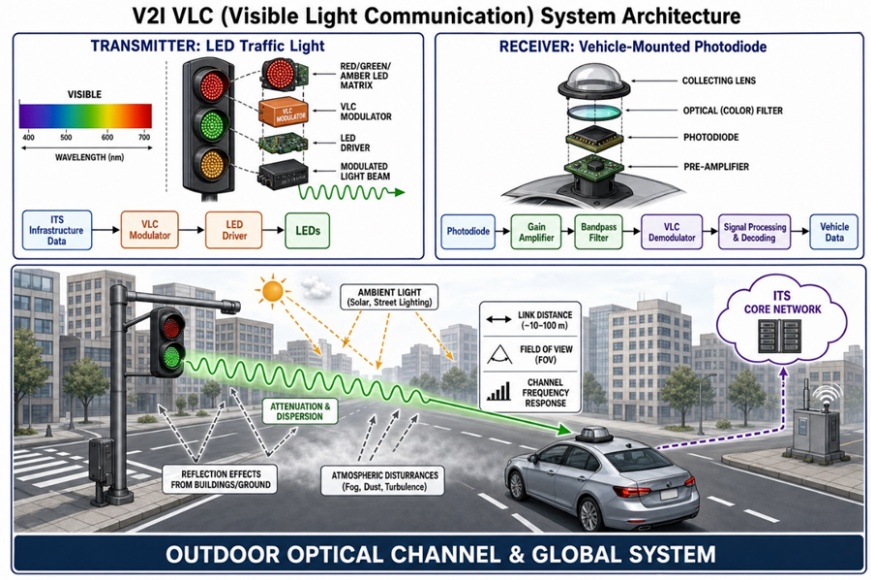


Figure 1.2: *Generic VLC-based V2I communication architecture for urban environments.*

Mobility introduces dynamic channel variations. As a vehicle moves, the distance to the transmitter changes continuously, the incidence angle varies, and periods of misalignment arise. At highway speeds, these changes occur rapidly and must be tracked by adaptive signal processing [8].

1.4 VLC-Based Positioning Techniques

The same optical channel that carries data in VLC also encodes spatial information. Received signal strength, time of arrival, and the angle of incidence all depend on the geometric relationship between transmitter and receiver. These dependencies can be exploited to estimate position [13].

1.4.1 Received Signal Strength (RSS) Positioning

RSS-based positioning exploits the fact that received optical power depends on the distance between transmitter and receiver. For a Lambertian LED source, the received power is given by [14]:

$$P_r = \frac{(m+1)A}{2\pi d^2} \cdot P_t \cdot \cos^m(\varphi) \cdot T_s(\psi) \cdot g(\psi) \cdot \cos(\psi) \tag{1.1}$$

where m is the Lambertian emission order, A is the photodiode effective area, d is the transmitter-receiver distance, φ is the irradiance angle at the transmitter, ψ is the angle of incidence at the receiver, $T_s(\psi)$ is the optical filter gain, and $g(\psi)$ is the optical concentrator gain.

The Lambertian order m is related to the LED half-power semi-angle $\Phi^{1/2}$ by:

$$m = -\frac{\ln(2)}{\ln\left(\cos(\Phi^{1/2})\right)} \tag{1.2}$$

Once the distance d is estimated from the received power, trilateration using measurements from at least three known LED positions yields the two-dimensional receiver coordinates. RSS methods require no clock synchronization and are inexpensive. However, they are sensitive to environmental variability: changes in receiver orientation, ambient light contamination, and reflection effects all alter the received power without a corresponding change in position [13].

1.4.2 Time-Based Positioning: TOA and TDOA

Time of Arrival (TOA) positioning estimates distance from the propagation delay of the optical signal. The distance is [13]:

$$d = c \cdot \tau \tag{1.3}$$

where $c = 3 \times 10^8$ m/s is the speed of light and τ is the measured propagation delay. At the speed of light, a 1 ns timing error translates into a 30 cm distance error. Achieving sub-meter accuracy therefore demands picosecond-to-nanosecond timing precision.

Time Difference of Arrival (TDOA) measures the difference in arrival times from two transmitters at the same receiver, rather than absolute propagation delays. This removes the need for receiver absolute clock synchronization. With measurements from at least three transmitters, hyperbolic positioning locates the receiver in two dimensions [13].

1.4.3 Angle of Arrival (AOA) Positioning

AOA positioning estimates the direction from which an optical signal arrives at the receiver. Using imaging sensors or arrays of multiple photodiodes, the angular distribution of received light intensity reveals the bearing angle to each transmitter. Triangulation from two or more bearing angles yields the receiver's two-dimensional coordinates [13].

AOA methods do not require strict timing and can achieve good accuracy without knowing the absolute transmit power. However, they demand more complex hardware and involve higher computational cost.

1.4.4 Limitations in Dynamic Urban Environments

All three approaches assume that a direct LoS link exists between the LED transmitter and the vehicle receiver. In real urban environments, this assumption frequently fails. Other vehicles,

trucks, and temporary obstructions regularly block direct LoS paths. Furthermore, classical positioning algorithms assume a static or quasi-static scenario. At vehicular speeds, the geometric relationship changes within milliseconds, making static algorithms insufficient [8].

Table 1.1: *Comparative Overview of VLC-Based Positioning Methods*

Method	Accuracy	Sync. Required	Hardware Cost	Urban Robustness
RSS	0.1 – 1 m	No	Low	Moderate
TOA	< 0.1 m (ideal)	Strict	High	Low
TDOA	0.1 – 0.5 m	Inter-Tx only	Medium	Moderate
AOA	0.1 – 0.3 m	No	High	Moderate
Fingerprint	0.1 – 0.5 m	No	Medium	High (trained)

1.5 Optical Retroreflection

Retroreflection is a specific optical phenomenon in which light is returned almost exactly toward its source, regardless of surface orientation — within a defined angular acceptance range. This differs fundamentally from specular reflection and diffuse reflection. The directional return property makes retroreflection highly interesting for vehicular VLC positioning: a single vehicle can emit light, receive the return, and derive range information — all without any active transmitter on the roadside [15, 16].

1.5.1 Physical Principles and Mathematical Modeling

Two primary physical mechanisms implement retroreflection in practice. The first is the corner cube retroreflector, which consists of three mutually perpendicular reflective surfaces forming the interior corner of a cube. A light ray entering the corner cube undergoes exactly three reflections. Each reflection inverts one component of the propagation direction vector. If the incident ray direction is $\mathbf{k} = (k_x, k_y, k_z)$, the three successive reflections produce the outgoing vector $-\mathbf{k}$, perfectly reversing the direction of propagation for any angle of incidence within the mechanical aperture [15].

The second mechanism relies on transparent glass microspheres. The incoming ray refracts at the front surface, reflects off the rear metallized surface, and refracts again upon exiting. For a sphere with the right refractive index, these operations combine to return light toward the source. Bead-based retroreflectors are less precise than corner cubes but are inexpensive and suitable for large-area coatings such as road markings and traffic signs [15].

For LED-based VLC, the key parameter is the effective received power after retroreflection. A simplified link budget model for a retroreflective VLC channel can be written as:

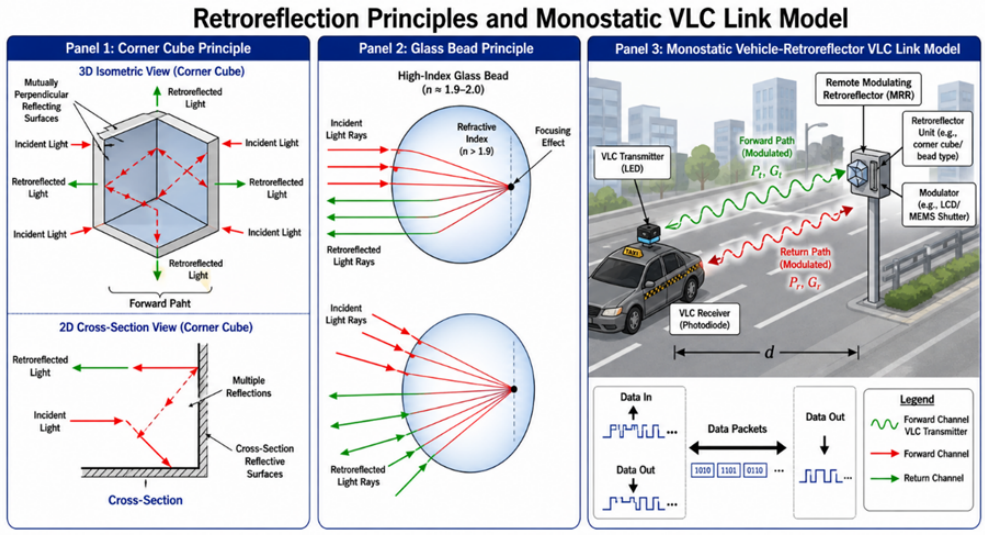


Figure 1.3: *Physical principles of optical retroreflection and the monostatic vehicular VLC link model.*

$$P_r = P_t \cdot H_{\text{out}}(d, \varphi, \psi) \cdot \rho_r \cdot H_{\text{ret}}(d, \varphi, \psi) \tag{1.4}$$

where P_t is the transmitted optical power, H_{out} represents the forward channel gain from the vehicle to the retroreflector (governed by the Lambertian model), ρ_r is the retroreflection coefficient of the surface, and H_{ret} is the return channel gain back to the vehicle receiver. In a monostatic configuration, where transmitter and receiver are co-located on the same vehicle, the combined round-trip power decays as $1/d^4$:

$$P_r \propto \rho_r \cdot \cos^{2m}(\varphi) \cdot \frac{\cos^2(\psi)}{d^4} \tag{1.5}$$

This $1/d^4$ dependence directly enables range estimation from received power measurements, analogous to radar range equations. It also implies that retroreflective VLC operates over relatively short distances, typically up to a few tens of meters, which is consistent with urban vehicular safety applications [16].

1.5.2 Existing Applications in Transportation

Retroreflective materials are already ubiquitous in road environments. Traffic signs, lane markings, delineator posts, guardrail reflectors, and raised pavement markers all rely on retroreflection to return vehicle headlight beams toward the driver. This passive visibility mechanism requires no external power and significantly reduces nighttime accident rates compared to non-reflective equivalents [15].

The critical practical implication for this work is that retroreflective infrastructure already exists at scale in most urban road networks. Every traffic sign and every lane marking is a

potential optical landmark that can reflect a vehicle-mounted LED signal back toward the vehicle, without any electrical connection or maintenance of electronic components [16].

In optical wireless research, retroreflective backscatter communication has been demonstrated in laboratory settings, showing that passive retroreflective surfaces can support not just ranging but also data communication by modulating their reflectivity. These results confirm that retroreflective surfaces are capable of serving as integrated positioning and communication elements [16, 17].

1.5.3 Interest for Passive Low-Complexity VLC Positioning

The combination of existing retroreflective road infrastructure and the monostatic architecture it enables makes retroreflection especially attractive for vehicular VLC positioning.

- **No active infrastructure required:** Retroreflective road markers and signs need no power supply, synchronization circuits, or communication modules on the roadside.
- **Built-in synchronization:** In a monostatic configuration, the same vehicle unit transmits and receives the signal. No external clock synchronization is needed, eliminating the main source of TOA-based positioning error.
- **Spatial selectivity:** Because retroreflectors return light toward the source, only the transmitting vehicle receives a strong return signal, reducing co-channel interference from neighboring vehicles.
- **Wavelength compatibility:** Retroreflection in geometric optics is wavelength-independent within the visible spectrum. Retroreflective materials designed for white headlights respond equally well to modulated LED sources in the VLC band [15].
- **Complementarity with GNSS:** Retroreflective VLC can provide precise short-range distance references in exactly the environments where GNSS is most degraded — dense urban canyons.

1.6 VLC Channel Estimation and Its Link to Localization

Channel estimation is a fundamental component of any VLC system. In the context of vehicular positioning, it takes on an additional role: the parameters of the estimated channel directly encode the spatial relationship between transmitter and receiver. This section presents the propagation models, estimation techniques, and the mechanisms by which channel parameters can be translated into position information [12, 18].

1.6.1 Optical Propagation Models in Urban Environments

The foundation of VLC channel modeling is the Lambertian source model. A typical LED emits optical intensity that follows [14]:

$$I(\varphi) = I_0 \cdot \cos^m(\varphi) \tag{1.6}$$

The direct line-of-sight (LoS) DC channel gain between a single LED and a photodetector is [14]:

$$H_{\text{LoS}} = \frac{(m+1)A}{2\pi d^2} \cdot \cos^m(\varphi) \cdot T_s(\psi) \cdot g(\psi) \cdot \cos(\psi), \quad \psi \leq \psi_c \tag{1.7}$$

In real outdoor environments, the full channel impulse response (CIR) includes the direct LoS component and contributions from multiple reflections [12]:

$$h(t) = h_{\text{LoS}}(t) + \sum_i h_{\text{ref},i}(t) \tag{1.8}$$

Each reflected component carries its own delay τ_i and attenuation factor α_i, determined by the reflector geometry and surface reflectance. For the retroreflective case, the CIR contains an additional component arriving with round-trip delay $\tau_{\text{rr}} = 2d/c$. Because this component arrives after nearby surface reflections, it is in principle separable in the time domain when the range d is sufficient [12, 16].

1.6.2 Channel Estimation Techniques in VLC

Pilot-based estimation inserts known training sequences into the transmitted signal. In OFDM-based VLC systems, pilot subcarriers enable frequency-domain channel estimation using Least Squares (LS) or Minimum Mean Square Error (MMSE) algorithms [9, 18].

Time-domain impulse response estimation uses short optical pulses or pseudo-random binary sequences as probing signals. By cross-correlating the received signal with a replica of the transmitted sequence, the impulse response is estimated directly. This technique is particularly valuable for ranging applications, since the peak of the cross-correlation directly yields the propagation delay τ and hence the distance $d = c\tau$.

Adaptive filtering algorithms such as Least Mean Squares (LMS) and Recursive Least Squares (RLS) update channel estimates iteratively to track time-varying conditions. These methods are well-suited to vehicular VLC, where the channel changes continuously due to vehicle motion [12].

Machine learning-based estimators, including deep neural networks, have also been applied to VLC channel estimation. They learn the mapping from received signals to channel parameters directly from data, showing particular promise in handling strong ambient noise.

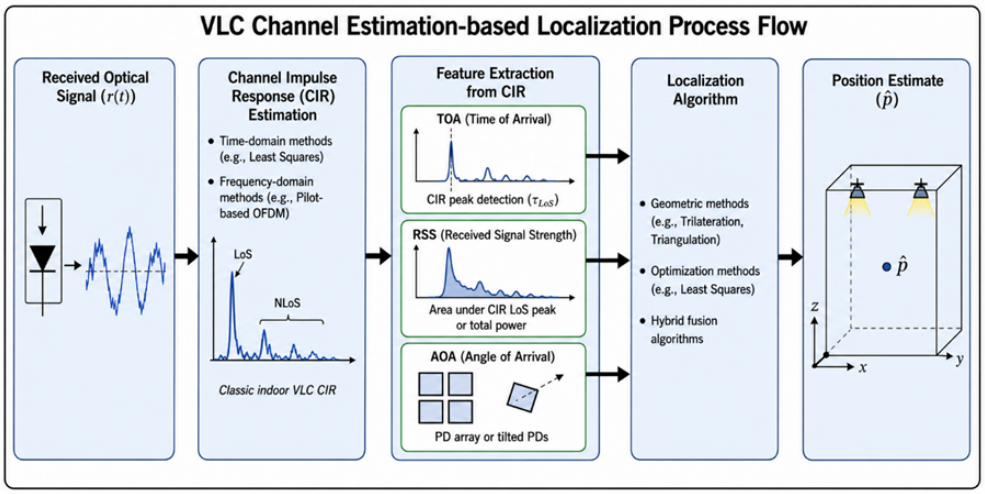


Figure 1.4: *Channel estimation pipeline for VLC-based localization*

However, their computational cost and need for large training datasets remain challenges for real-time vehicular applications.

1.6.3 Channel Parameters as Sources of Position Information

The key insight linking channel estimation to positioning is that several measurable channel parameters are deterministic functions of the transmitter-receiver geometry [13, 18].

- **Channel DC gain (RSS):** The received power P_r depends on d^{-2}, φ, and ψ through Eq. (1.1) and (1.7). Inverting this relationship gives an estimate of the range d, forming the basis of RSS positioning.
- **Propagation delay (TOA):** The time of the first arriving peak in the impulse response corresponds to direct path delay $\tau = d/c$. High-resolution time-domain estimation gives direct range measurements.
- **Angle of incidence (AOA):** Using an array of photodetectors with different orientations, the angular distribution of received intensity encodes the direction of arrival.
- **Multipath profile fingerprinting:** The full shape of the CIR is a spatial fingerprint. In urban environments, each location generates a somewhat unique delay-power profile that can be matched against a pre-recorded database [13].
- **RMS delay spread:** The temporal spread of the impulse response depends on the surrounding reflection geometry and provides indirect information about the vehicle's environment.

For the retroreflective VLC case, the key observable is the round-trip delay τ_{rr} of the retroreflected component, which gives the range as $d = c \cdot \tau_{\text{rr}}/2$. The monostatic configuration eliminates external synchronization requirements, making this TOA estimate fundamentally cleaner than in distributed active systems. This constitutes one of the central technical advantages exploited by the proposed approach.

1.7 Critical Review of the State of the Art

Vehicular Visible Light Communication has attracted sustained research interest over the past decade. Pioneering studies established the technical feasibility of both Vehicle-to-Vehicle (V2V) and Vehicle-to-Infrastructure (V2I) optical links under realistic ambient light interference conditions, demonstrating that appropriate optical filtering combined with equalization techniques could sustain reliable communication over short-to-medium transmission ranges. Subsequently, research efforts shifted toward system-level challenges, including adaptive modulation schemes and hybrid RF/VLC architectures designed to mitigate the performance degradation induced by Line-of-Sight (LoS) blockage events [8]. A major contribution to the field was provided by Memedi and Dressler, whose comprehensive survey of the vehicular VLC literature systematically identified the principal open challenges, among which robustness to dynamic traffic conditions, the absence of dedicated standardization frameworks, and the need for seamless integration with existing automotive communication platforms were highlighted as critical priorities [8]. Notwithstanding this body of work, significant research gaps persist. The majority of experimental investigations have been conducted either under controlled laboratory conditions or in clear daylight environments, with little to no systematic treatment of adverse meteorological conditions. Furthermore, multi-vehicle network scenarios and interference management strategies between adjacent VLC links remain largely unexplored in the existing literature.

Channel estimation for VLC systems has been extensively investigated, primarily in the context of indoor optical wireless communications. Classical estimators, including Least Squares (LS) and Minimum Mean Square Error (MMSE) algorithms tailored to VLC Intensity Modulation/Direct Detection (IM/DD) architectures, have demonstrated satisfactory performance under quasi-static channel conditions. For vehicular environments, Kalman filter-based estimators have been proposed as a means to track the rapidly time-varying channel characteristics induced by vehicle motion. More recently, deep learning-based approaches trained on simulated vehicular channel datasets have exhibited enhanced robustness against ambient noise and channel non-stationarity [12, 18]. However, several important limitations remain unaddressed in the current state of the art. Most published contributions assume moderate vehicle speeds, and the extension to high-speed scenarios representative of highway environments has received insufficient attention. Moreover, the lack of a standardized vehicular VLC channel model constitutes a fundamental obstacle to the rigorous cross-comparison of estimation techniques across independent publications.

The application of retroreflective technology to VLC-based localization is an emerging and largely unexplored research direction, with only a limited number of published contributions available to date. Schmid et al. provided a proof-of-concept demonstration of retroreflective VLC in a controlled indoor laboratory environment, establishing that pas-

Table 1.2: *Comparison of Related Works in VLC and Retroreflective Systems*

Reference	Focus Area	Environment	Retroreflection	Limitation
Hassan et al. [14]	V2V VLC link	Outdoor road	No	No adverse weather treatment
Jin et al. [14]	LED-to-PD VLC	Road (100 m)	No	Daytime conditions only
Ghasemi et al. [13]	Channel estimation	Indoor / low mobility	No	Performance degradation at high speed
Wang et al. [13]	Kalman-based tracking	Vehicular (simulated)	No	Restricted to moderate speed
Zhang et al. [18]	Retroreflective positioning	Indoor only	Yes	No outdoor channel model
Schmid et al. [17]	Retro-VLC backscatter	Indoor short-range	Yes	No vehicular context
This Work	**Retro-VLC positioning + channel estimation**	**Outdoor urban vehicular**	**Yes**	**—**

sive modulated retroreflectors are capable of sustaining short-range optical communication without requiring active transmitters at the tag node [16].

Building upon this foundation, Zhang et al. extended the retroreflective VLC paradigm to the problem of indoor localization, achieving decimeter-level positioning accuracy through the combined use of modulated retroreflective tags and a single LED illuminator [17].

Nevertheless, the transition from indoor laboratory conditions to outdoor vehicular environments introduces a fundamentally different set of challenges: the solar background radiation significantly degrades the Signal-to-Noise Ratio (SNR) of the retroreflected return signal, moving reflectors introduce wide dynamic range variations, and no outdoor channel model for retroreflective VLC has been established to date.

Table 1.2 provides a structured summary of the most relevant works identified in this review, confirming the existence of a well-defined and previously unaddressed research gap.

1.8 Conclusion

This chapter introduced the technical background and motivation of the work. GNSS is insufficient in dense urban environments, which motivates the use of VLC for vehicular localization due to its accuracy potential and robustness to electromagnetic interference. However, existing VLC positioning systems rely on active infrastructure, limiting practical

deployment.

To overcome this limitation, optical retroreflection is proposed to turn passive road elements into positioning landmarks. A vehicle can estimate distance using round-trip optical signals without external synchronization, making the approach simpler and more scalable.

The literature review shows that retroreflective VLC has only been studied in indoor scenarios, with no existing outdoor channel models or vehicular localization solutions validated in real conditions. This highlights a clear research gap.

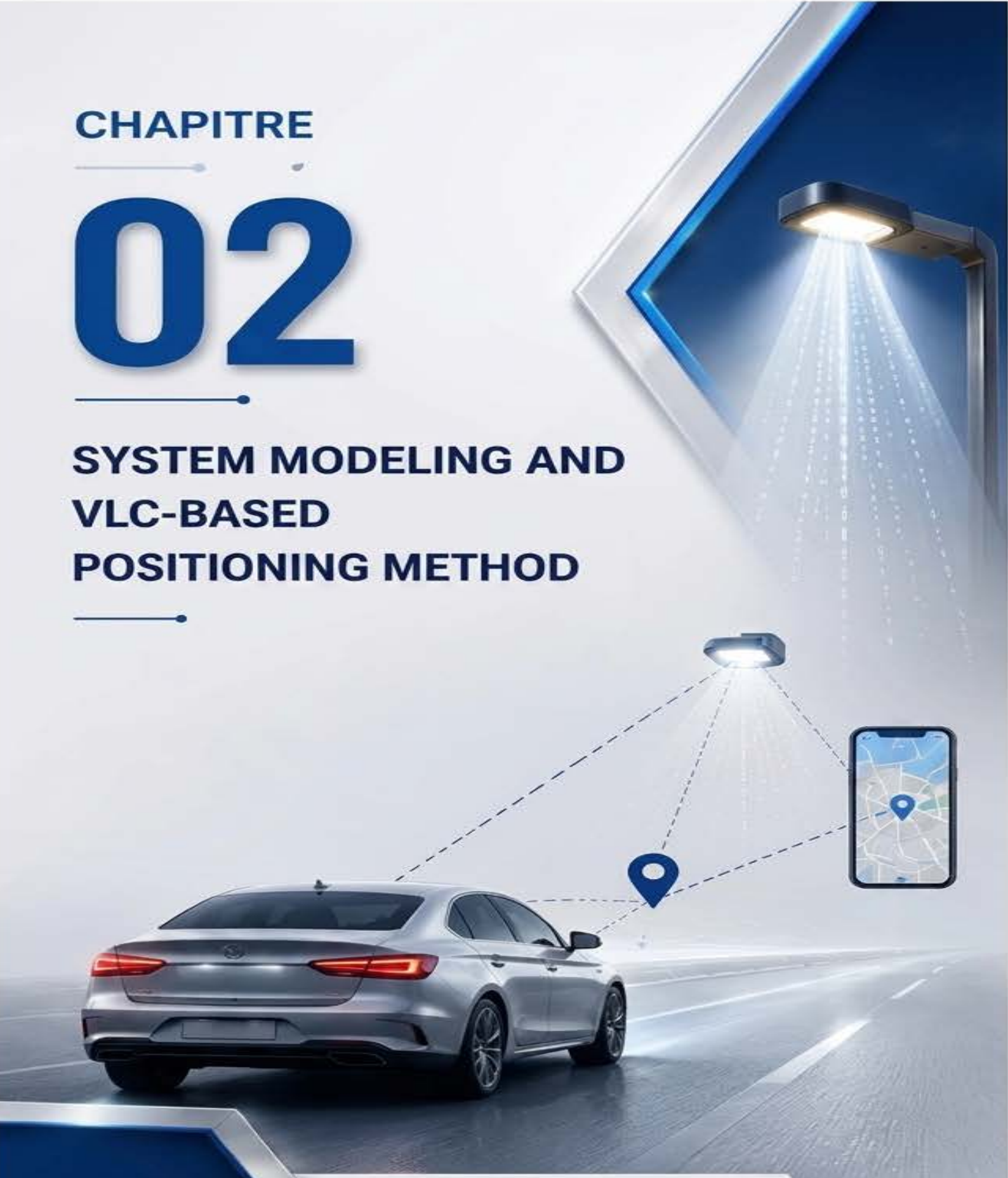
The problem addressed is therefore the development of a robust retroreflective VLC-based localization system for urban environments where GNSS is unreliable. This requires modeling the outdoor channel, designing reliable channel estimation and ranging methods, and evaluating system performance for ITS requirements.

The next chapters present the system and channel model, the proposed estimation algorithms, and finally the simulation and experimental validation results.

CHAPITRE

02

SYSTEM MODELING AND VLC-BASED POSITIONING METHOD



- System Model
- VLC Channel Model
- Positioning Algorithm
- Implementation Framework

Chapter 2

System Modeling and VLC-Based Positioning Method

2.1 Introduction

Chapter 1 established the theoretical foundations of Visible Light Communication (VLC) for vehicular positioning, highlighted the limitations of GNSS in dense urban environments, and identified a clear research gap in the use of retroreflective VLC for outdoor vehicular scenarios. In particular, the monostatic link concept and the round-trip optical propagation law (Eq. (1.4)–(1.5)) were introduced as the basis of the proposed framework. Building on these elements, the present chapter develops a complete and mathematically consistent system model that enables rigorous analysis and practical implementation.

The chapter is structured as follows. Section 2.2 presents the overall vehicular VLC architecture and defines the geometric relationships between the system components. Section 2.3 derives the complete optical channel model, including the forward Lambertian propagation, the retroreflection mechanism using corner-cube retroreflectors (CCRs), and the noise characteristics under outdoor conditions. Section 2.4 formulates the received signal model at the angle diversity receiver (ADR) and defines the associated channel estimation problem. Finally, Section 2.5 introduces the positioning framework, detailing its mathematical formulation, the nonlinear optimization approach, and its extension to multi-CCR configurations.

2.2 Architecture of the Proposed Vehicular VLC System

2.2.1 System Overview

The proposed system is designed for vehicle-to-vehicle (V2V) communication and positioning in a head-to-tail road scenario, as illustrated in Figure 2.1. Two vehicles share the same lane: Vehicle A (the transmitting vehicle) and Vehicle B (the target vehicle). The objective is for Vehicle A to simultaneously determine its distance from Vehicle B and estimate the optical channel between them, without any active transmitter being required on Vehicle B

and without a dedicated feedback link [19, 8].

The architecture relies on three functional components:

1. the optical transceiver assembly on Vehicle A, combining LED transmitters for illumination and data transmission with an angle diversity receiver (ADR) for retroreflected signal capture,
2. passive retroreflective elements installed on the rear surface of Vehicle B,
3. the photodiode array on Vehicle B for conventional downlink reception.

The key innovation lies in the monostatic configuration of Vehicle A, which uses the same optical signal for both downlink communication and round-trip ranging without any modification to the transmitted waveform [19, 20].

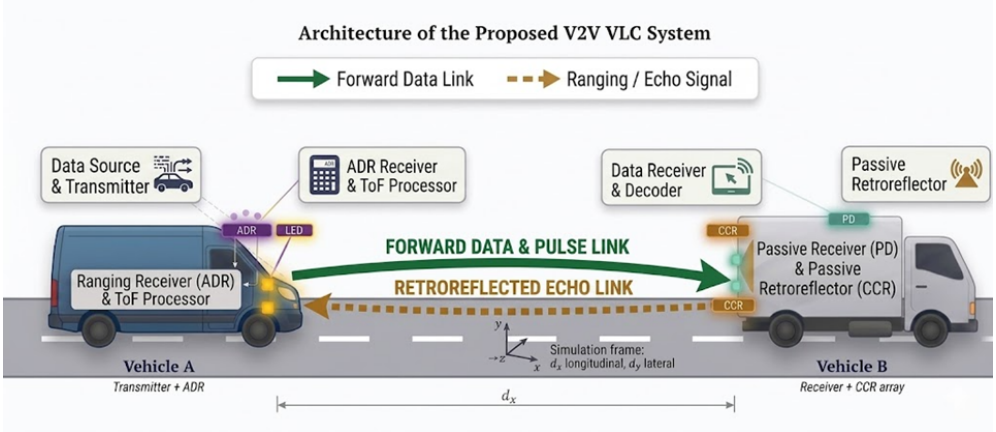


Figure 2.1: *Complete architecture of the proposed retroreflective V2V VLC positioning system.*

2.2.2 LED Transmitter Assembly

Vehicle A is equipped with J LED sources, indexed $j = \{1, \ldots, J\}$, forming the headlight array (Figure 2.2). Each LED provides both visible illumination and optical data transmission through intensity modulation. In the baseline scenario, $J = 2$ LEDs are considered, corresponding to the left and right headlights of a standard vehicle. The inter-headlight separation distance is denoted d_l, and the position vector of the j-th LED is defined as $\mathbf{l}_j$. Without loss of generality, the coordinate system is centered on the first headlight, so that $\mathbf{l}_1 = [0, 0]$ and $\mathbf{l}_2 = [0, d_l]$ [19, 14].

Each LED is characterized by its half-power semi-angle $\Phi^{1/2}$ which determines the Lambertian emission order m (introduced in Chapter 1, Eq. (1.2)). Vehicle headlights exhibit an asymmetric radiation pattern in practice; however, the Lambertian approximation with $\Phi^{1/2} = 60°$ provides a reasonable model for the low beam, as confirmed by the analysis in [19]. The total transmitted optical power per LED is P_t (W), which is also the illumination power. No additional pilot or sensing power budget is required; the positioning function is

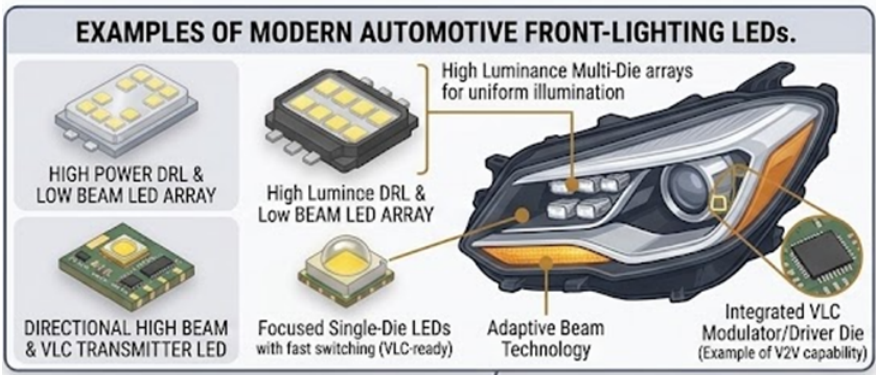


Figure 2.2: *Exemple of modern automotive front-lighting LEDs.*

embedded within the standard illumination and communication signal [14, 21].

2.2.3 Angle Diversity Receiver (ADR)

The ADR is the central hardware element that enables retroreflective positioning. It is mounted on Vehicle A, co-located with the first LED headlight ($j = 1$). The ADR consists of N photodiodes (PDs), indexed $i = \{1, \ldots, N\}$, each oriented in a distinct direction in the azimuthal plane. The angular orientation of the i-th PD is denoted α_i, and the corresponding pointing vector is $\mathbf{v}_i$. Each PD is equipped with a Compound Parabolic Concentrator (CPC) to maximize received power within its designated field-of-view (FoV) (Figure 2.3) [19, 22].

The rationale for using an ADR rather than a single wide-angle PD is twofold. First, a single PD with a wide FoV would receive strong ambient light noise, severely degrading the SNR of the weak retroreflected signal. Second, a single PD provides only one scalar measurement, which is insufficient to simultaneously estimate the two-dimensional position vector of Vehicle B. By combining multiple PDs oriented in different directions, the ADR provides a vector of measurements whose angular content encodes the direction of arrival (DoA) of the retroreflected signal, enabling full 2D positioning through Angle of Arrival (AoA) techniques [13, 22].

2.2.4 Passive Retroreflective Element (CCR)

Vehicle B carries no active optical transmitter. Instead, one or more corner-cube retroreflectors (CCRs) are installed along its rear bumper. A single CCR is assumed in the baseline configuration, centered at the mid-width of the vehicle. The CCR is a passive optical element: it consumes no electrical power, requires no synchronization signal, and introduces no processing latency. Its sole function is to return incident optical energy toward the source with minimal angular deviation (Figure 2.4) [15, 23, 24].

The geometric parameters of the CCR are its diameter D_{cc} and its length L_{cc}. These

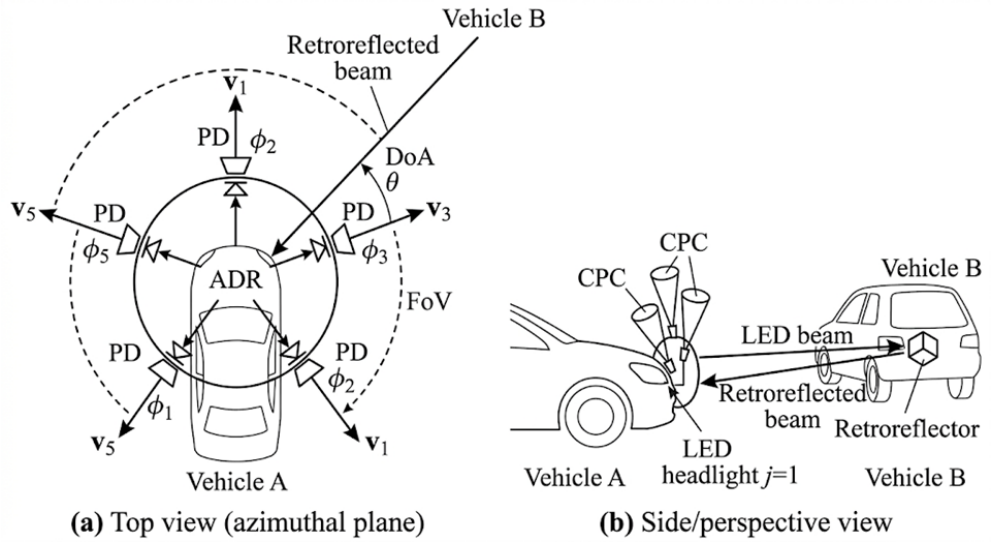


Figure 2.3: *Diagram of the ADR system and retro-reflection-based VLC positioning principle.*

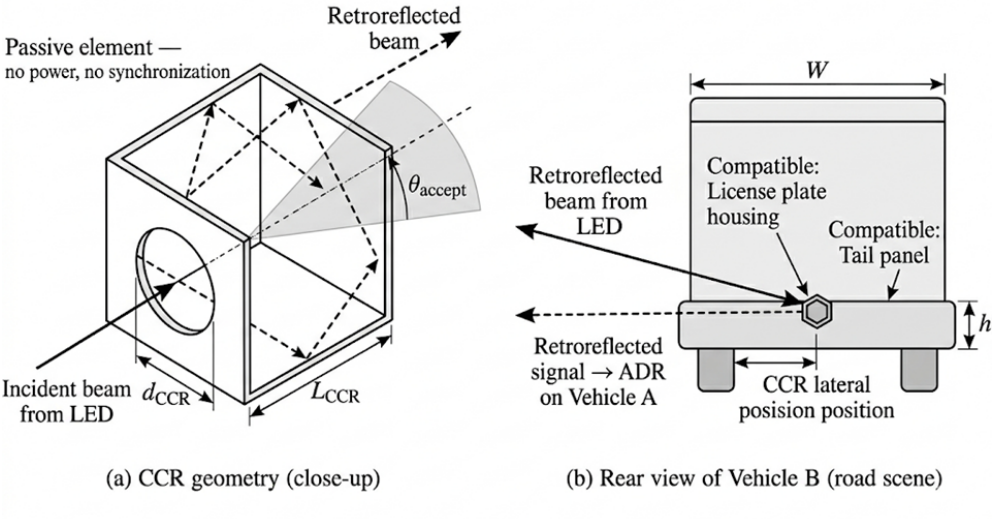


Figure 2.4: *Geometric Analysis and Automotive Integration of a Corner-Cube Retroreflector (CCR) for Passive VLC Positioning.*

dimensions determine the effective retroreflective area, the angular acceptance range, and the optical gain of the element. Their impact on the received signal power is derived in Section 1.5.1. In road environments, CCRs are already embedded in rear bumper reflectors, license plate illumination housings, and truck tail panels, suggesting that the proposed system architecture is compatible with existing automotive standards [19, 23].

2.3 VLC Channel Modeling with Retroreflection

2.3.1 Lambertian Line-of-Sight Forward Model

The propagation model for the direct optical path between LED j on Vehicle A and PD k on Vehicle B follows the Lambertian LoS channel gain model introduced in Chapter 1 (Eq. (1.7)). For completeness and to fix notation used throughout this chapter, the channel gain of the LoS component is recalled without re-derivation H_{LoS} (see Eq. (1.7)), where $d_{j,k}$ is the Euclidean distance from LED j to PD k, θ_j is the radiation angle of LED j with respect to its optical axis, $\phi_{j,k}$ is the incidence angle at PD k, A_k is the effective area of PD k, and m is the Lambertian emission order (Eq. (1.2) of Chapter 1). $T_s(\psi)$ and $g(\psi)$ are the optical filter transmittance and concentrator gain, respectively. The LoS component accounts for approximately 95% of the total received optical power in VLC links, which justifies neglecting the non-LoS contribution in channel computation [14, 19].

The radiation angle θ_j of LED j toward the CCR position $\mathbf{u} = [d_x, d_y]$ is computed as:

$$\theta_j = \cos^{-1}\left(\frac{d_x}{\|\mathbf{d}_j\|}\right) \tag{2.1}$$

where $\mathbf{d}_j = \mathbf{u} - \mathbf{l}_j$ is the distance vector from the j-th LED to the CCR, and $\|\mathbf{d}_j\|$ is its Euclidean norm. This formulation is directly employed in the positioning algorithm of Section 2.5 [19].

2.3.2 Corner-Cube Retroreflector (CCR) Model

A corner-cube retroreflector (CCR) consists of three mutually orthogonal flat mirrors that return an incident ray exactly antiparallel to itself over a wide acceptance cone. The mathematical properties of the triple-reflection mechanism have been analyzed in detail in [15, 24]. The relevant quantity for the channel model is the effective reflective area ε of the CCR as seen by an incoming ray at incidence angle θ. For a circular CCR of diameter D_{cc}, this ratio is given by [19, 24]:

$$\varepsilon = \frac{2D_{\text{cc}}\left(\cos^{-1}\left(\frac{D}{2D_{\text{cc}}}\right) - \frac{D}{2D_{\text{cc}}}\sin\left(\cos^{-1}\left(\frac{D}{2D_{\text{cc}}}\right)\right)\right)}{\pi D_{\text{cc}}^2} \tag{2.2}$$

where $D = 2L_{\text{cc}}\tan(\Phi)$ is a geometry-dependent variable, L_{cc} is the length of the CCR, and Φ is the refraction angle at the entry face of the CCR. Following Snell's law:

$$\Phi = \arcsin\left(\frac{\eta_1 \sin\theta}{\eta_2}\right) \tag{2.3}$$

where η_1 and η_2 are the refractive indices of the external medium (air, $\eta_1 = 1$) and the

CCR material, respectively. The maximum diameter of the CCR is constrained by its length through:

$$D_{\text{cc}}^{\max} = \frac{2L_{\text{cc}}}{\sqrt{2}} \tag{2.4}$$

and the corresponding maximum physical area is:

$$A_{\text{cc}}^{\max} = \frac{L_{\text{cc}}^2 \pi}{2} \tag{2.5}$$

Equations (2.2)–(2.5) fully characterize the geometrical efficiency of the CCR as a function of the incidence angle. The parameter ε takes values in $[0, 1]$ and decreases as the incidence angle θ deviates from the optical axis of the CCR. For the positioning application, this angular sensitivity is exploited by the ADR to extract directional information [19, 23].

2.3.3 Retroreflected Channel Gain

The retroreflected optical signal travels from LED j on Vehicle A, strikes the CCR on Vehicle B, and returns to the ADR photodiode i on Vehicle A. This round-trip path is characterized by a composite channel gain. Under the assumption that the CCR position and the ADR are co-located with the first LED headlight (i.e., all PDs in the ADR are considered to have position vector $\mathbf{l}_1$ for the purpose of range estimation), the retroreflected channel gain at PD i is [19, 20]:

$$h_i^{\text{Ret}} = \frac{(m+1)}{8\pi (d_i)^2} A_i \cos^m(\theta) \cos(\phi_i) G_i \varepsilon, \quad \phi_i \leq \psi_i \tag{2.6}$$

where $d_i = |\mathbf{u} - \mathbf{l}_1|$ is the Euclidean distance from the first LED (and the co-located ADR) to the CCR, ϕ_i is the incidence angle of the i-th PD, G_i is the optical gain provided by the CPC of PD i, ψ_i is the individual FoV half-angle of PD i, and ε is the effective reflective area factor of the CCR defined in Eq. (2.2). This expression differs from the forward LoS gain (Eq. (1.7)) in two important ways: (i) the denominator contains d_i^2 rather than $d_{j,k}^2$, because the monostatic path already accumulates a $1/d^2$ decay in each direction, yielding an effective $1/d^4$ scaling consistent with Eq. (1.5) of Chapter 1; and (ii) the CCR efficiency ε introduces an additional angular dependence that encodes directional information [14, 19].

The factor $c = \frac{(m+1)A_i}{8\pi} G_i$ groups the constant system parameters. With this notation, the received optical power at PD i can be written compactly as:

$$P_{r_i} = \beta \rho P_t C \frac{1}{\|\mathbf{d}_i\|^2} \left(\frac{d_x}{\|\mathbf{d}_i\|} \right)^m \left(\frac{\mathbf{d}_i \cdot \mathbf{v}_i}{\|\mathbf{d}_i\| \|\mathbf{v}_i\|} \right) \varepsilon + n_i \tag{2.7}$$

where $\beta \in [0, 1]$ is the reflecting loss factor of the CCR surface, ρ is the photodiode responsivity, $\mathbf{v}_i$ is the known orientation unit vector of PD i in the ADR, d_x is the longitudinal

distance between the vehicles, and n_i is the additive noise component. Equation (2.7) is the fundamental sensing equation of the proposed positioning system: it establishes a nonlinear relationship between the measured power P_{r_i} and the unknown vehicle position vector $\mathbf{u} = [d_x, d_y]$ [19].

2.3.4 Communication Channel at Vehicle B

In parallel with the retroreflective sensing path, the direct downlink channel between LED j on Vehicle A and PD k on Vehicle B serves for data communication. The transmit signal at LED j is formed as:

$$x_j = w_{k,j} s_j + p_j \tag{2.8}$$

where s_j is the data symbol intended for the receiving vehicle, p_j is the DC bias required to satisfy the non-negativity constraint of optical intensity modulation, and $w_{k,j}$ is the (k, j) element of the precoding matrix $\mathbf{W} \in \mathbb{R}^{K \times J}$. The dynamic range constraint on the LED requires:

$$\sum_{j=1}^{M} \|w_{k,j}\| \leq \tilde{p}_j, \quad \tilde{p}_j = \min(p_j, p_{\max} - p_j) \tag{2.9}$$

At PD k on Vehicle B, after DC removal, the received signal is:

$$y_k = \rho_k \sum_{j=1}^{J} h_{k,j} x_j + n_k \tag{2.10}$$

where $h_{k,j}$ is the forward channel gain from Eq. (1.7) and n_k is the total noise at PD k. The signal model in Eq. (2.10) is identical in form to that of Chapter 1 but is now connected to the channel estimation procedure of Section 2.4 through the estimated matrix $\hat{\mathbf{H}}$ [19, 25].

2.3.5 Noise Modeling

The total noise at any photodiode in this system — whether in the ADR on Vehicle A or in the PD array on Vehicle B — follows Gaussian statistics and is characterized by its variance σ^2, which is the sum of two independent contributions: shot noise and thermal noise [26, 27].

a) Shot Noise

Shot noise arises from the random arrival of photons at the photodetector and is the dominant noise term in outdoor VLC due to background solar and ambient light. Its variance is [26, 27]:

$$\sigma^2_{\text{shot}} = 2qI_{\text{bg}}B \tag{2.11}$$

where $q = 1.6 \times 10^{-19}$ C is the electronic charge, B is the modulation bandwidth, and I_{bg} is the photocurrent generated by background illumination, defined as:

$$I_{\text{bg}} = A_i G \int_{\lambda_1}^{\lambda_2} P_{\text{bg}}(\lambda) T_f(\lambda) d\lambda \tag{2.12}$$

Here, λ is the wavelength variable over the optical bandpass $[\lambda_1, \lambda_n]$, G is the CPC gain, $T_f(\lambda)$ is the optical filter transmittance, and $P_{\text{bg}}(\lambda)$ is the spectral background radiance. The latter depends strongly on time of day and atmospheric conditions: for full daylight, a solar spectral irradiance of approximately $P_{\text{solar}} \approx 1500$ W/(m$^2 \cdot \mu$m) is assumed, while for night-time (full moon), $P_{\text{moon}} \approx 0.005$ W/(m$^2 \cdot \mu$m) [19, 27, 28]. The shot noise therefore varies by several orders of magnitude between daytime and nighttime operation, which has a direct and significant impact on positioning accuracy, as analysed in Section 2.3.3.

b) Thermal Noise

Thermal noise arises from resistive elements in the receiver front-end circuit, primarily the load resistor R_L of the transimpedance amplifier. Its variance is:

$$\sigma^2_{\text{thermal}} = \frac{4 k_B T_k}{R_L} B \tag{2.13}$$

where $k_B = 1.38 \times 10^{-23}$ J/K is Boltzmann's constant and T_k is the absolute temperature in Kelvin. In outdoor vehicular VLC, the shot noise variance given by Eq. (2.11) typically exceeds the thermal noise variance by several orders of magnitude during daytime, making shot noise the limiting factor [26, 29].

c) Total Noise Variance and SNR

The total noise variance at PD i is the sum of both contributions:

$$\sigma_i^2 = \sigma^2_{\text{shot}} + \sigma^2_{\text{thermal}} \tag{2.14}$$

The instantaneous Signal-to-Noise Ratio (SNR) at PD i of the ADR for the retroreflected signal is then:

$$\text{SNR}_i = \frac{(\rho \beta P_t h_i^{\text{Ret}})^2}{\sigma_i^2} \tag{2.15}$$

Equation (2.15) reveals the fundamental trade-off in retroreflective VLC positioning: increasing P_t or using larger CPC gains improves the SNR, but the background-driven shot noise grows with the receiver aperture area A_i. The optimal CPC design must therefore balance gain against noise area. This trade-off is explored in the ADR design in Sec-

tion 2.3.2 [19, 28, 29].

2.4 Signal Model and Channel Estimation at the ADR

2.4.1 ADR Signal Measurement Vector

Let $\mathbf{P} = [P_{r_1}, P_{r_2}, \ldots, P_{r_N}]^\mathsf{T}$ denote the vector of received optical power measurements collected from the N photodiodes of the ADR. Each component P_{r_i} is given by Eq. (2.7). The complete nonlinear measurement model can be written in vector form as:

$$\mathbf{P} = \mathbf{f}(\mathbf{u}) + \mathbf{n} \tag{2.16}$$

where $\mathbf{f} : \mathbb{R}^2 \to \mathbb{R}^N$ is the nonlinear measurement function whose i-th component is defined by Eq. (2.7), $\mathbf{u} = [d_x, d_y]^\mathsf{T}$ is the unknown position vector of Vehicle B, and $\mathbf{n} = [n_1, n_2, \ldots, n_N]^\mathsf{T}$ is the noise vector with components $n_i \sim \mathcal{N}(0, \sigma_i^2)$. The system has two unknowns (d_x and d_y) and N equations. For a unique solution to exist, at least two PDs must simultaneously receive the retroreflected signal, i.e., at least two components of $\mathbf{P}$ must be non-zero [19].

The probability that at least two PDs simultaneously capture the retroreflected signal depends on the ADR design parameters: the number of PDs N, their individual FoV ψ, and the overlap factor O_v between adjacent FoVs. This probability is a key design criterion and is analyzed in Section 2.3.2 [19, 22].

2.4.2 Compound Parabolic Concentrator (CPC) Design

Each PD in the ADR is coupled with a Compound Parabolic Concentrator (CPC)(Figure 2.5), a non-imaging optical device that concentrates incoming light from a wide acceptance cone onto the small photodiode surface. The optical gain provided by the CPC to PD i is [19, 22]:

$$G(\phi_i) = \begin{cases} \left(\frac{D_1}{D_2}\right)^2 = \frac{\eta^2}{\sin^2 \psi_i}, & \phi_i \le \psi_i \\ 0, & \phi_i > \psi_i \end{cases} \tag{2.17}$$

where η is the refractive index of the CPC material, D_1 and D_2 are the entrance and exit aperture diameters of the CPC, respectively, and ψ_i is the FoV half-angle of PD i. For a circular CPC, the entrance area is $A_i = \pi D_1/4$ and the photodiode area is $A_{\text{PD}} = \pi D_2/4$. The physical length of the CPC is:

$$L_{\text{CPC}} = \frac{(D_1 + D_2)\cot\psi}{2} \tag{2.18}$$

The total FoV of the ADR, denoted Ψ_{ADR}, is apportioned among the N PDs according to:

$$\psi_i = \frac{\Psi_{\text{ADR}}}{N - \frac{1}{2}O_v(N-1)} \tag{2.19}$$

where $O_v \in [0, 1]$ is the overlap factor between adjacent PD FoVs. When $O_v = 0$, the FoVs are non-overlapping and the ADR covers the full angular range with no redundancy. When $O_v = 1$, each PD's FoV fully overlaps with its neighbors, maximizing the probability that the retroreflected signal is captured by multiple PDs simultaneously [19, 22].

The angular orientation α_i of the i-th PD in the azimuthal plane is assigned as:

$$\alpha_i = \begin{cases} \dfrac{(2i - 1 - N)}{2}\psi, & N \text{ even} \\ (i - N_{\text{odd}})\psi, & N \text{ odd} \end{cases} \tag{2.20}$$

where $N_{\text{odd}} = \text{round}(N/2)$. The corresponding orientation unit vector $\mathbf{v}_i$ used in Eq. (2.7) is:

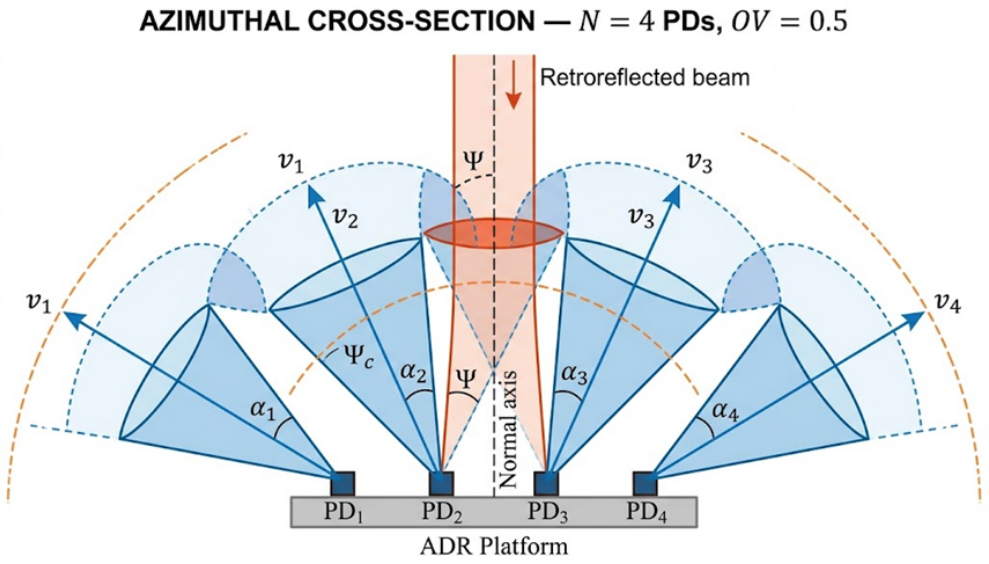


Figure 2.5: *ADR geometric configuration showing CPC-coupled photodiodes and their angular orientations*

$$\mathbf{v}_i = [\cos\alpha_i,\ \sin\alpha_i] \tag{2.21}$$

Equations (2.17)–(2.21) fully specify the ADR geometry. The CPC parameters D_1, D_2, and L_{CPC} scale with $1/\sin(\psi_i)$, so reducing the individual FoV (i.e., increasing N for fixed Ψ_{ADR}) increases the CPC dimensions and the ADR bulk. The trade-off between compactness, coverage probability, and SNR is a central ADR design problem analyzed for the purpose of this thesis but whose quantitative results are presented in Chapter 3 [19].

2.4.3 Sensitivity Analysis: Distance and Angular Effects

The sensitivity of the received retroreflected power P_{r_i} to the vehicle's position can be analyzed by examining the partial derivatives of Eq. (2.7) with respect to the position components d_x and d_y. The longitudinal sensitivity with respect to d_x reflects the range estimation capability, while the lateral sensitivity with respect to d_y encodes the lateral displacement information needed for full 2D positioning.

From Eq. (2.7), the power P_{r_i} depends on d_x both through the distance $\|\mathbf{d}_i\| = \sqrt{d_x^2 + d_y^2}$ and through the projection $d_x/\|\mathbf{d}_i\|$ that appears in the Lambertian emission factor. The partial derivative with respect to the longitudinal distance is:

$$\frac{\partial P_{r_i}}{\partial d_x} = \beta \rho P_t C \varepsilon \, \frac{\partial}{\partial d_x} \left(\frac{d_x^m}{\|\mathbf{d}_i\|^{m+2}} \left(\frac{\mathbf{d}_i \cdot \mathbf{v}_i}{\|\mathbf{d}_i\| \|\mathbf{v}_i\|} \right) \right) \tag{2.22}$$

The explicit evaluation of this derivative reveals that for a purely aligned configuration ($d_y = 0$), the power decays monotonically with increasing d_x, providing unambiguous range information. For a lateral offset $d_y \neq 0$, the projection $\frac{\mathbf{d}_i \cdot \mathbf{v}_i}{\|\mathbf{d}_i\| \|\mathbf{v}_i\|}$ introduces a directional weighting that differs across the N PDs, thereby encoding the lateral displacement [19].

The sensitivity degrades at long distances due to the $1/\|\mathbf{d}_i\|^4$ power law, limiting the effective operating range of the retroreflective positioning system. Additionally, at large lateral offsets, one or more PDs may exit the acceptance cone of the CCR ($\phi_i > \psi_i$), causing their received power to drop to zero. Maintaining adequate coverage probability under maximum lateral displacement (up to $d_y = d_{y,\max}$) imposes a lower bound on the ADR total FoV Ψ_{ADR} [19].

2.4.4 Robustness to Ambient Perturbations

In outdoor vehicular environments, the dominant perturbation to the retroreflective signal is background illumination noise. Its statistical impact was modeled in Section 2.3.5 through the shot noise variance (Eq. (2.11)). From the SNR expression in Eq. (2.15), it follows that a minimum SNR threshold $\text{SNR}_{\min}$ must be maintained at all PDs for the measurement vector $\mathbf{P}$ to carry sufficient information for positioning.

During daytime operation, the solar background current I_{bg} can reach several milliamperes per square centimeter of detector area, which overwhelms the small retroreflected photocurrent generated over distances beyond approximately 10–15 m. This places a hard constraint on the maximum operational range during daylight. Night-time operation is substantially more favorable: background illumination is dominated by street lamps and vehicle taillights, reducing I_{bg} by three to four orders of magnitude relative to the solar case [28, 29].

Additional perturbations include: (i) angular misalignment, arising when the vehicle follows a curved trajectory and the retroreflector departs from the nominal azimuthal plane;

(ii) surface contamination of the CCR reducing β; and (iii) inter-vehicle interference from adjacent VLC emitters. The monostatic architecture provides inherent robustness against point (iii), since retroreflectors return light only toward the incident source. Points (i) and (ii) are mitigated by the CPC overlap design ($O_v > 0$) and by the use of robust estimation algorithms described in Section 2.5 [19, 21, 30].

2.5 Positioning Method Based on Channel Estimation

2.5.1 Mathematical Formulation of the Positioning Problem

The positioning problem is formulated as a nonlinear least-squares problem. Given the N-dimensional measurement vector $\mathbf{P} = [P_{r_1}, \ldots, P_{r_N}]^\mathsf{T}$ collected at the ADR, the objective is to find the position vector $\hat{\mathbf{u}} = [\hat{d}_x, \hat{d}_y]^\mathsf{T}$ that best explains the observations. The formal problem statement is:

$$\hat{\mathbf{u}} = \arg\min_{\mathbf{u}} \sum_{i=1}^{N} \frac{(P_{r_i} - f_i(\mathbf{u}))^2}{\sigma_i^2} \tag{2.23}$$

where $f_i(\mathbf{u})$ is the nonlinear model of Eq. (2.7) evaluated at position $\mathbf{u}$. The weighted sum of squared residuals in Eq. (2.23) constitutes a Maximum Likelihood (ML) estimator under the Gaussian noise assumption of Eq. (2.14) [13, 19].

The function $f_i(\mathbf{u})$ is smooth and differentiable almost everywhere, but the problem is nonconvex: multiple local minima may exist, particularly when N is small or when the SNR is low. A good initialization strategy is therefore essential for convergence to the global minimum. The selection of the initial point $\hat{\mathbf{u}}^0$ is discussed in Section 2.5.3 [19].

2.5.2 Levenberg–Marquardt Algorithm

The Levenberg–Marquardt (LM) algorithm is adopted to solve the nonlinear least-squares problem of Eq. (2.23). The LM algorithm is a trust-region method that interpolates between the Gauss-Newton step and the gradient descent step, providing reliable convergence even when the initial guess is distant from the solution [19].

Let $\mathbf{r}(\mathbf{u}) = \mathbf{P} - \mathbf{f}(\mathbf{u})$ be the residual vector and $\mathbf{J}(\mathbf{u}) = \frac{\partial \mathbf{f}}{\partial \mathbf{u}} \in \mathbb{R}^{N\times 2}$ the Jacobian matrix of $\mathbf{f}$ with respect to the position vector $\mathbf{u}$. The LM update rule at iteration k is:

$$\mathbf{u}^{(k+1)} = \mathbf{u}^{(k)} + \left(\mathbf{J}^\mathsf{T}\mathbf{W}\mathbf{J} + \lambda_k \mathbf{I}\right)^{-1} \mathbf{J}^\mathsf{T}\mathbf{W}\,\mathbf{r}(\mathbf{u}^{(k)}) \tag{2.24}$$

where $\mathbf{W} = \mathrm{diag}(1/\sigma_1^2, \ldots, 1/\sigma_N^2)$ is the noise-weighted matrix, $\lambda_k > 0$ is the LM damping parameter, and $\mathbf{I}$ is the 2×2 identity matrix. When λ_k is large, the update reduces to a scaled gradient descent step, ensuring stability. When λ_k is small, the update approximates

the Gauss-Newton step, providing fast convergence near the solution. The damping parameter is updated adaptively based on the reduction in the cost function at each iteration [19].

The Jacobian $\mathbf{J}(\mathbf{u})$ is evaluated analytically from the partial derivatives of Eq. (2.7). For the i-th row:

$$\mathbf{J}_i(\mathbf{u}) = \left[\frac{\partial f_i}{\partial d_x}, \frac{\partial f_i}{\partial d_y} \right] \tag{2.25}$$

The partial derivatives can be obtained by differentiating Eq. (2.7) symbolically. Their expressions depend on the geometry of the CCR (through ε and its derivative with respect to the incidence angle ϕ_i) and on the Lambertian model (through the projection factor $\mathbf{d}_i \cdot \mathbf{v}_i$).

The convergence criterion of the LM algorithm is:

$$\|\mathbf{u}^{(k+1)} - \mathbf{u}^{(k)}\| < \varepsilon_{\text{tol}} \quad \text{or} \quad k < k_{\max} \tag{2.26}$$

where ε_{tol} is the convergence tolerance (typically set to 10^{-6} m) and $k_{\max}$ is the maximum number of iterations. The localization error is then defined as the Euclidean distance between the true position $\mathbf{u}$ and the estimated position $\hat{\mathbf{u}}$:

$$\Delta\mathbf{u} = \|\mathbf{u} - \hat{\mathbf{u}}\| \tag{2.27}$$

Equation (2.27) serves as the primary performance metric for the positioning module and is evaluated statistically through Monte Carlo simulation in Chapter 3 [19].

2.5.3 Initialization Strategy

The initial estimate $\hat{\mathbf{u}}^0$ for the LM algorithm can be obtained from a simple RSS-based ranging approach. Using the total received power at the ADR (sum of all PD measurements), an initial estimate of the range $\|\mathbf{d}_1\|$ can be obtained by inverting Eq. (2.7) under the aligned assumption ($d_y = 0$):

$$\|\mathbf{d}_1\|^0 \approx \left[\frac{\beta \rho P_t C \varepsilon_0}{\sum_{i=1}^{N} P_{r_i}} \right]^{1/2} \tag{2.28}$$

where ε_0 is the CCR efficiency evaluated at $\theta = 0$. The initial lateral offset is set to $\hat{d}_y^0 = 0$. This aligned initialization provides a coarse but reliable starting point that lies within the basin of attraction of the global minimum for typical inter-vehicular distances (5–30 m) and lateral offsets (0–10 m), as verified through simulation analysis [19].

2.5.4 Channel Estimation from Positioning

Once the position estimate $\hat{\mathbf{u}} = [\hat{d}_x, \hat{d}_y]^\mathsf{T}$ has been obtained from the LM algorithm, it is used to estimate the direct-link optical channel between the LED array of Vehicle A and the PD array of Vehicle B. The estimated distance from LED j to PD k is:

$$\hat{d}_{k,j} = \left| (\hat{\mathbf{u}} \pm \mathbf{d}_k) - \mathbf{l}_j \right| \tag{2.29}$$

where $\mathbf{d}_k$ represents the known offset between the k-th PD and the CCR in the lateral direction on Vehicle B. Substituting $\hat{d}_{k,j}$ into the Lambertian model, the estimated channel coefficient is [19]:

$$\hat{h}_{k,j} = \begin{cases} \dfrac{(m+1)A_k}{2\pi \hat{d}_{k,j}^2} \cos^m(\hat{\theta}_j) \cos(\hat{\phi}_{k,j}), & \hat{\phi}_{k,j} \le \psi_c \\ 0, & \hat{\phi}_{k,j} > \psi_c \end{cases} \tag{2.30}$$

where $\hat{\theta}_j$ and $\hat{\phi}_{k,j}$ are the estimated radiation and incidence angles derived from $\hat{\mathbf{u}}$. The complete estimated channel matrix is $\hat{\mathbf{H}} \in \mathbb{R}^{K \times J}$ with elements $\hat{h}_{k,j}$. This position-derived channel estimate is a key contribution of the proposed system: it eliminates the need for pilot symbols and closed-loop feedback, which typically introduce both overhead and latency in vehicular VLC systems [19, 21, 31].

2.5.5 Zero-Forcing Precoding Based on Estimated CSI

The estimated channel matrix $\hat{\mathbf{H}}$ is fed into a zero-forcing (ZF) precoding scheme at the transmitter. ZF precoding inverts the channel to suppress inter-user interference. The precoding matrix $\mathbf{W}$ is computed as [19, 25]:

$$\hat{\mathbf{H}}\mathbf{W} = \mathrm{diag}(\lambda_k) \tag{2.31}$$

where λ_k is the effective channel gain at receiver k after precoding. In practice, the Moore-Penrose pseudo-inverse is used:

$$\mathbf{W} = \hat{\mathbf{H}}^\mathsf{T}(\hat{\mathbf{H}}\hat{\mathbf{H}}^\mathsf{T})^{-1} \mathrm{diag}(\lambda_k) \tag{2.32}$$

Since $\mathbf{W}$ is computed from the estimated matrix $\hat{\mathbf{H}}$ and applied to the real channel $\mathbf{H}$, the ZF precoders do not perfectly null the interference. The residual interference depends on the accuracy of $\hat{\mathbf{H}}$, which in turn depends on the positioning error $\Delta\mathbf{u}$. The resulting sum spectral efficiency (SSE) is given by:

$$\mathrm{SSE} = \log_2 \det\left(\mathbf{I} + \frac{P_t}{\sigma_k^2}|\hat{\mathbf{H}}\mathbf{W}|^2\right) \tag{2.33}$$

Equation (2.33) is the end-to-end performance metric connecting the positioning accuracy to the communication quality of service. It is employed in Chapter 3 to assess the impact of the estimation accuracy on the achievable spectral efficiency [19, 25].

2.5.6 Generalization to Multiple CCRs

The single-CCR scenario analyzed above is the baseline case. When multiple retroreflective beacons are available — for example, when the vehicle ahead carries two CCRs at known relative positions, or when multiple vehicles in the platoon are simultaneously retroreflecting — the measurement model can be extended straightforwardly.

Suppose that M CCRs are present, located at positions $\mathbf{u}^1, \mathbf{u}^2, \ldots, \mathbf{u}^M$ relative to Vehicle A. Each CCR contributes an independent set of retroreflected signals to the ADR. The total received power at PD i is the superposition:

$$P_{r_i} = \sum_{m=1}^{M} f_i(\mathbf{u}_m) + n_i \tag{2.34}$$

If the contributions from different CCRs can be separated — for example, through time-division, frequency-division, or code-division multiplexing of the transmit signal — then a separate position estimate $\hat{\mathbf{u}}_m$ can be obtained for each beacon. These estimates can be fused using weighted least-squares to improve overall positioning accuracy:

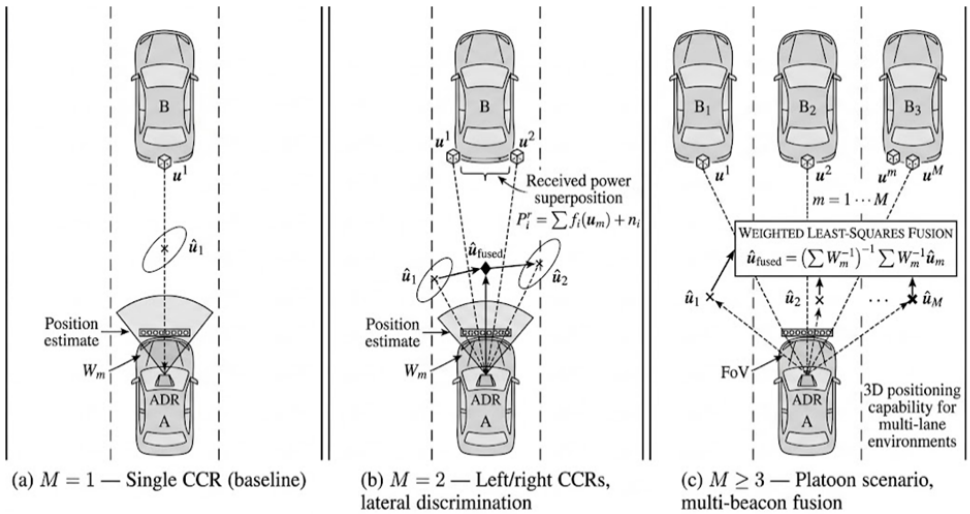


Figure 2.6: *Multi-CCR generalization of a retroreflection VLC positioning.*

$$\hat{\mathbf{u}}_{\text{fused}} = \left(\sum_{m=1}^{M} \mathbf{W}_m^{-1} \right)^{-1} \sum_{m=1}^{M} \mathbf{W}_m^{-1} \hat{\mathbf{u}}_m \tag{2.35}$$

where $\mathbf{W}_m$ is the covariance matrix of the positioning error for the m-th beacon estimate. This multi-beacon fusion follows the cooperative localization framework reviewed in Chapter 1[6, 19].

In the simplest scenario, $M = 1$ and the baseline single-CCR model applies. $M = 2$ corresponds to a vehicle with a left-side and a right-side CCR, providing additional lateral discrimination. $M \geq 3$ begins to offer three-dimensional positioning capability, relevant for multi-lane environments [6, 20].

2.6 Conclusion

This chapter presented the complete mathematical framework of the proposed retroreflective VLC system for positioning and channel estimation.

A V2V architecture without an active transmitter on the target vehicle was introduced, relying on a monostatic ADR-based sensing approach. The retroreflected channel model and noise characterization were developed consistently with the system geometry.

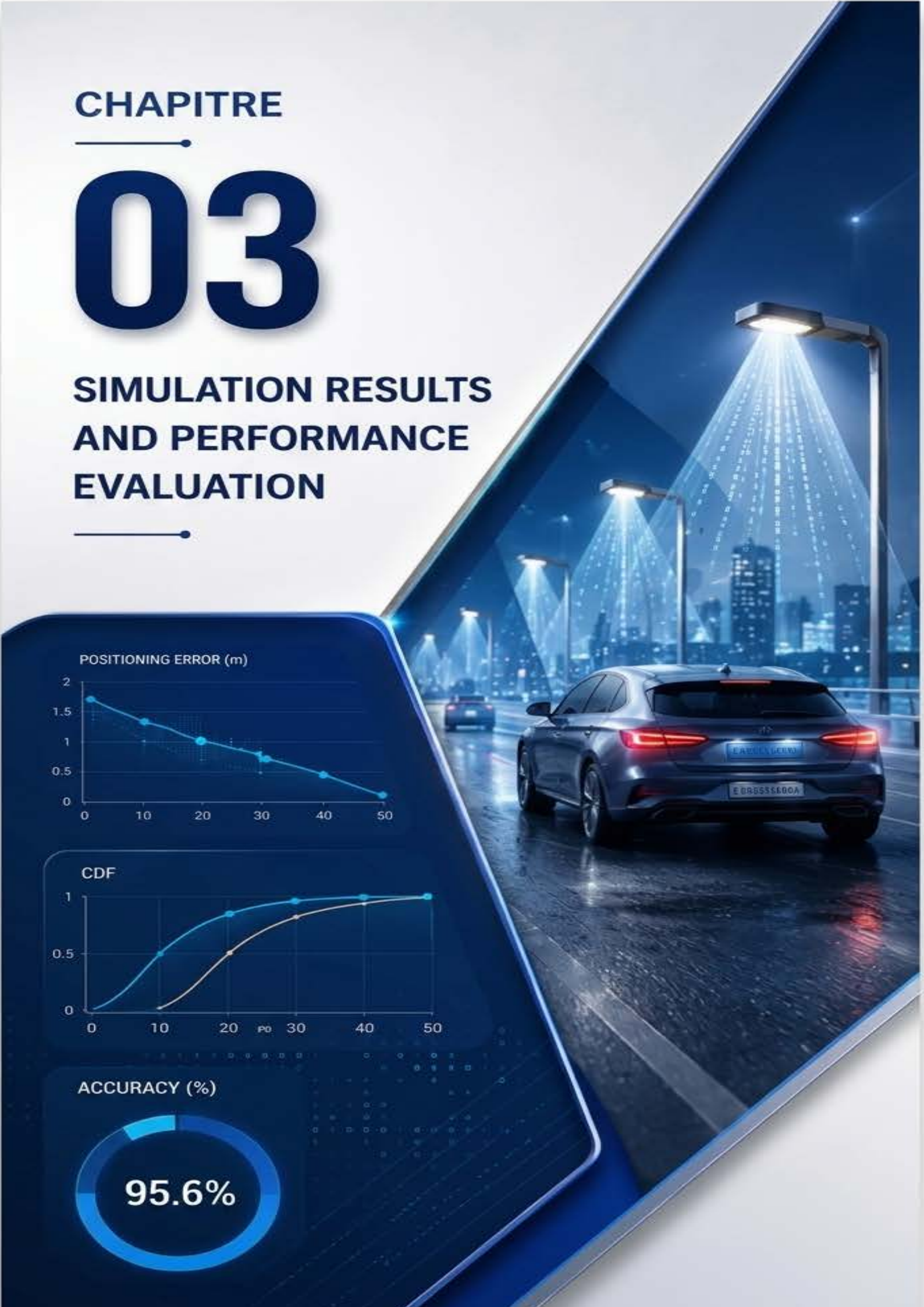
The ADR design and the localization problem were formulated and solved using a nonlinear least-squares approach based on the Levenberg–Marquardt algorithm. The estimated position is then used for channel reconstruction and precoding without feedback or pilot signaling. A multi-CCR extension was also introduced.

Finally, the next chapter evaluates system performance through Monte Carlo simulations in terms of localization error and spectral efficiency.

CHAPITRE

03

SIMULATION RESULTS AND PERFORMANCE EVALUATION



Chapter 3

Simulation Results and Performance Evaluation

3.1 Introduction

This chapter presents a comprehensive performance evaluation of the proposed retroreflective Visible Light Communication (VLC) system for vehicle-to-vehicle (V2V) positioning through Monte Carlo simulation. The simulation environment faithfully replicates the complete physical model of the system: the Lambertian forward channel, the Corner-Cube Retroreflector (CCR) angular efficiency, the Compound Parabolic Concentrator (CPC) optical gain, the shot and thermal noise model at the receiver front-end, and the nonlinear least-squares positioning algorithm solved via the Levenberg–Marquardt (LM) method.

To support the interactive exploration and validation of the proposed system, a dedicated MATLAB-based graphical simulation interface was developed. This tool, described in Section 3.3, provides a unified environment in which all physical models and performance metrics can be evaluated and visualised in real time, offering direct insight into the behaviour of the system across its full operational parameter space prior to the formal statistical analysis.

Performance is assessed over the full operational parameter space, covering inter-vehicle distances lateral offsets, ADR array sizes , and overlap factors, under both daytime and nighttime illumination conditions. Six performance metrics are evaluated for each configuration: the received SNR, the measurement error at the ADR photodiodes, the coverage probability, the CPC optical gain, the Euclidean positioning error, and the Sum Spectral Efficiency (SSE) under Zero-Forcing precoding.

3.2 Simulation Parameters

The simulation considers an inter-vehicular distance d_x ranging from 5 to 30 m and a lateral displacement d_y from 0 to 10 m. The Lambertian emission order $m = 1$ corresponds to a half-power semi-angle $\Phi_{1/2} = 60°$, the standard model for automotive low-beam headlights [14]. The thermal noise floor $\sigma^2_{\text{th}} = \frac{4k_B T_k}{R_L} B \approx 6.62 \times 10^{-19}$ A^2 defines the minimum achievable noise level at the receiver front-end [26]. Table 3.1 summarises all system parameters.

Table 3.1: *Simulation parameters.*

Parameter	Symbol	Value
Transmit optical power	P_t	10 W
Modulation bandwidth	B	20 MHz
Lambertian emission order	m	1
CCR reflectivity	ρ	0.54
Lambertian half-angle	$\Phi_{1/2}$	60°
CPC refractive index	η_{CPC}	1.5
CCR refractive index (front)	η_1	1.0
CCR refractive index (back)	η_2	1.5
ADR photodiode area	A_{PD}	0.1×10^{-4} m^2
Communication PD area	A_k	1×10^{-4} m^2
ADR full FoV angle	Ψ_{ADR}	90°
Boltzmann constant	k_B	1.38×10^{-23} J/K
Receiver temperature	T_k	300 K
Load resistance	R_L	50 Ω
Electron charge	q_e	1.6×10^{-19} C
Optical filter transmittance	T_f	1
Daytime background irradiance	$P_{\text{bg,day}}$	1.5×10^{-1} W/m^2
Night-time background irradiance	$P_{\text{bg,ngt}}$	5×10^{-7} W/m^2
LED spacing	d_l	1.5 m
Number of transmit LEDs	J	2
Number of receive PDs	K	2
Monte Carlo trials	N_{mc}	400

3.3 Description of the VLC Simulation Interface

To validate the theoretical models and enable rapid parametric exploration, an interactive graphical user interface (GUI) was developed in MATLAB, referred to as the *VLC Positioning Simulator*. As illustrated in Figure 3.1, the interface is organised into three functional zones.

Zone 1 — Control Panel

The left panel consolidates all interactive controls and live telemetry. Four sliders provide real-time adjustment of the key scenario parameters: the longitudinal distance d_x, the lateral offset d_y, the number of ADR photodiodes N, and the overlap factor O_v. A dedicated seed field ensures the reproducibility of all Monte Carlo draws.

Below the sliders, a live metrics panel displays the true and estimated vehicle coordinates, the active photodiode count, the day and night-time SNR values, and the sum spectral efficiency. The Euclidean positioning error $\Delta u = \|\hat{\mathbf{u}} - \mathbf{u}\|$ is highlighted with a colour-coded severity indicator: green for $\Delta u \leq 10$ cm, orange for 10 cm $< \Delta u \leq 50$ cm, and red for $\Delta u > 50$ cm.

Three action buttons complete the panel: **RUN / UPDATE** computes the selected figure on demand; **RUN ALL SIM** executes all simulation figures sequentially; and **EXPORT** saves the current graphic at publication quality. A scrollable list box allows selection among six performance figures, categorised into live plots and on-demand paper figures.

Zone 2 — Live Scene Panel

The central panel provides a continuously refreshed top-view rendering of the V2V geometry. Vehicle A (blue) and Vehicle B (green) are represented as rectangles. The ADR field-of-view cones are coloured green when actively capturing the retroreflected signal, and grey otherwise. Three graphical overlays are common to all scenes: an orange square marks the true CCR position, a red cross indicates the Levenberg–Marquardt position estimate, and a dashed red line visualises the positioning error vector. The panel updates automatically upon any slider movement, providing immediate visual feedback on the system geometry.

Zone 3 — Analysis Figure Panel

The right panel is reserved for on-demand analysis figures. Six performance curves can be computed individually or in batch mode, covering SNR versus distance, CDF of positioning error, coverage probability $P(\geq 2$ PDs) versus overlap factor, CPC optical gain, and CDF of Sum Spectral Efficiency under Zero-Forcing precoding. Computed figures are cached and

retrieved instantly on subsequent selections, unless a system parameter or the random seed is modified.

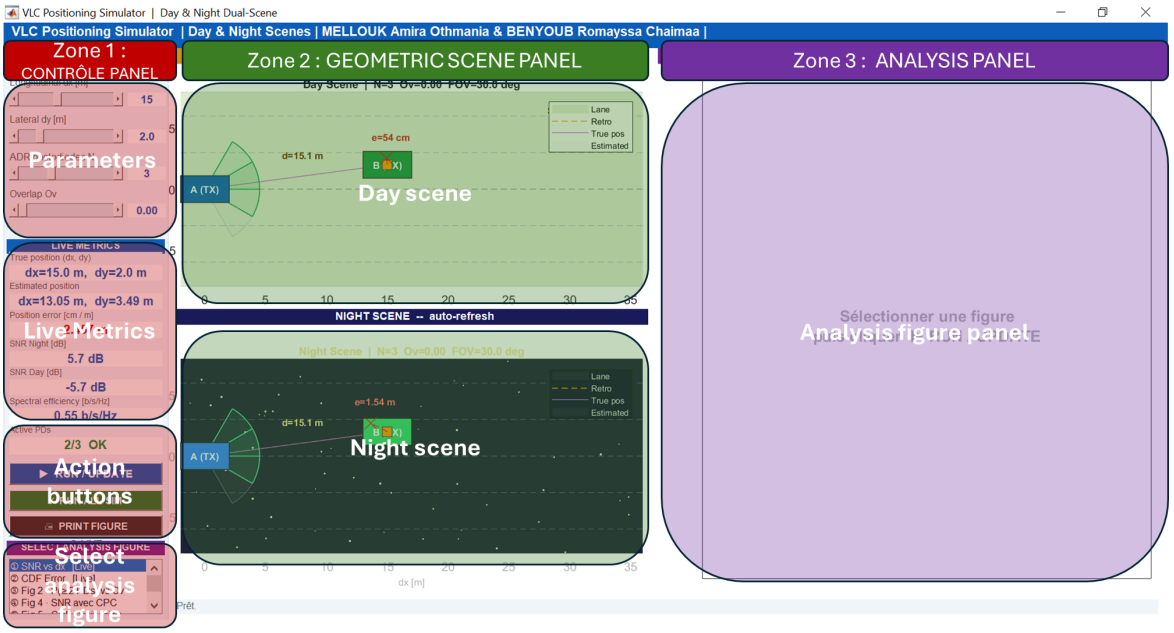


Figure 3.1: *Screenshot of the* VLC Positioning Simulator.

3.4 General Scenario Overview

The simulation environment represents a typical two-lane urban road segment in which two vehicles travel in the same direction. Vehicle A, referred to as the transmitting vehicle, is equipped with two LED headlights that form the optical transmitter array. An Angle Diversity Receiver (ADR) is mounted adjacent to the left headlight. Vehicle B, designated as the target vehicle, travels ahead of Vehicle A and is equipped with one or more passive Corner-Cube Retroreflectors (CCRs) mounted on its rear bumper, as well as a photodiode (PD) array for conventional downlink reception.

A Cartesian coordinate system is defined with its origin located at the midpoint of Vehicle A's headlight axis. The longitudinal x-axis is oriented along the direction of vehicle motion, whereas the lateral y-axis is perpendicular to the driving direction. Within this reference frame, the position of the CCR mounted on Vehicle B is represented by the coordinate vector $\mathbf{u} = [d_x, d_y]$, where d_x denotes the inter-vehicle distance and d_y corresponds to the lateral displacement between the centerlines of the two vehicles.

To evaluate system performance under representative traffic conditions, four distinct geometric configurations are considered. The first two configurations correspond to the aligned

driving scenario ($d_y = 0$), in which Vehicle B remains directly ahead of Vehicle A within the same lane. The remaining two configurations introduce a non-zero lateral displacement ($d_y \neq 0$), representing adjacent-lane operation or deviations caused by lane-keeping inaccuracies.

For each configuration, performance is evaluated under both daytime and nighttime ambient illumination conditions. The daytime background optical power density is set to $P_{\text{bg}} = 1500\,\text{W/(m}^2\cdot\mu\text{m)}$, whereas the nighttime condition is modeled with $P_{\text{bg}} = 0.005\,\text{W/(m}^2\cdot\mu\text{m)}$. The following performance metrics are investigated:

1. Signal-to-Noise Ratio (SNR) as a function of the longitudinal distance d_x;
2. Cumulative Distribution Function (CDF) of the raw measurement error observed at the ADR photodiodes;
3. Coverage probability, defined as $P(\geq 2\ \text{PDs})$, as a function of the overlap factor O_v;
4. SNR performance with Compound Parabolic Concentrator (CPC) gain compared with conventional photodiodes without CPC enhancement;
5. CDF of the Euclidean positioning error, $\Delta u = |\hat{\mathbf{u}} - \mathbf{u}|$;
6. CDF of the Sum Spectral Efficiency (SSE) achieved using Zero-Forcing (ZF) precoding.

All simulation results are obtained using $N_{\text{mc}} = 400$ Monte Carlo realizations for each operating point. During each realization, a vehicle position is randomly generated according to the considered configuration, and additive Gaussian noise is introduced based on the variance model described in Eq. (2.14). The Levenberg–Marquardt (LM) algorithm is then initialized using the RSS-based coarse position estimate $\hat{\mathbf{u}}_0$ defined in Eq. (2.28).

3.5 Case 1: Aligned Configuration

This sub-configuration constitutes the baseline reference for the entire evaluation. The nominal inter-vehicle distance of $d_x = 15$ m corresponds to a typical urban following scenario, and $N = 3$ is the minimum ADR array size that provides meaningful angular diversity beyond the bare two-photodiode case. $O_v = 0$ is used throughout this sub-configuration to isolate the contribution of the overlap factor, which is analysed systematically in Section 3.5.3.

The top-view scene corresponding to this configuration is shown in Figure 3.2. Two of the three ADR photodiode FoV cones successfully capture the retroreflected signal (green), while the third remains outside the acceptance cone of the CCR (grey). The LM position estimate (red cross) converges in close proximity to the true CCR location (orange square), providing a first visual confirmation of the algorithm's reliability under nominal night-time conditions at this geometry.

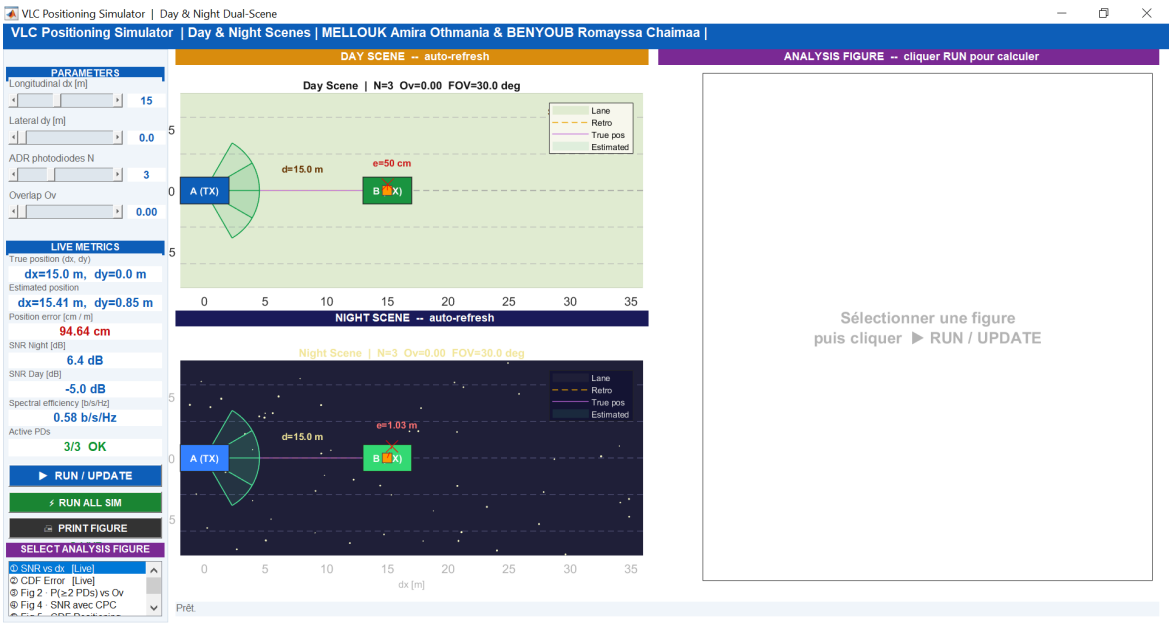


Figure 3.2: *Top-view scene: $d_x = 15$ m, $d_y = 0$ m, $N = 3$, $O_v = 0$. Green cones: active ADR FoV; grey: inactive. Orange square: true CCR position; red cross: LM estimate.*

3.5.1 SNR versus Distance

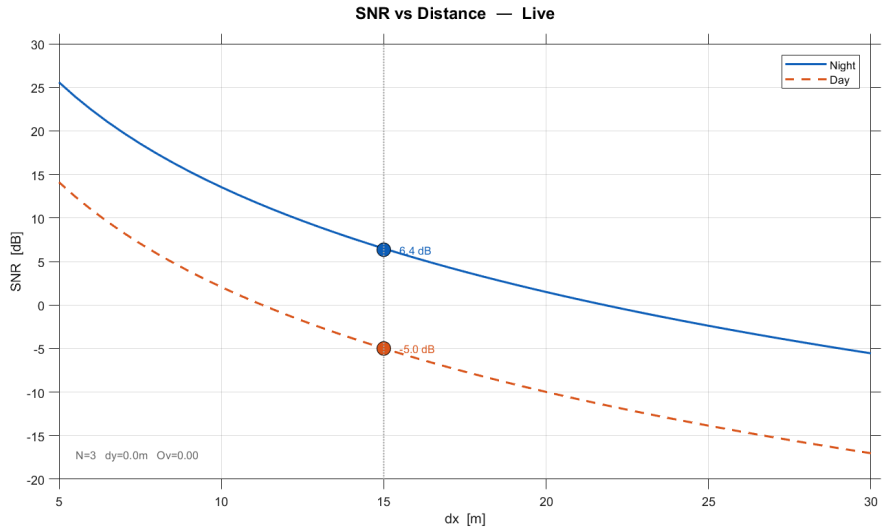
Figure 3.3 illustrates the average SNR at the ADR as a function of the longitudinal distance $d_x \in [5, 30]$ m for both overlap configurations ($O_v = 0$ and $O_v = 1$), under daytime and night-time conditions, with $N = 3$ and $d_y = 0$ m.

Under night-time conditions, the SNR decreases with distance according to the $1/|\mathbf{d}|^4$ round-trip path-loss model given in Eq. (1.5). At the reference distance of $d_x = 15$ m, the SNR reaches 6.4 dB for $O_v = 0$ (Figure 3.3a) and 0.3 dB for $O_v = 1$ (Figure 3.3b). In both cases, the SNR remains above 0 dB up to approximately 15 m, which is compatible with typical vehicle-following distances in intelligent transportation systems (ITS) [1, 2].

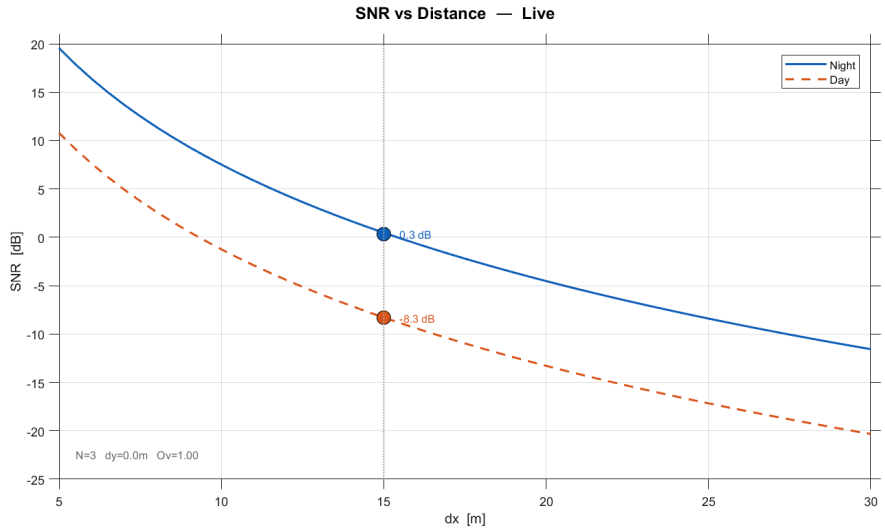
Although a larger overlap ratio is expected to benefit from the CPC optical gain, the configuration $O_v = 1$ exhibits a lower SNR than $O_v = 0$. This behavior results from the trade-off described in Eq. (2.17). Increasing O_v reduces the individual photodiode field-of-view (FoV) half-angle ψ_i, thereby increasing the CPC gain $G(\varphi_i) = \eta^2/\sin^2\psi_i$. However, the narrower FoV also decreases the likelihood that the retroreflected beam is simultaneously collected by several photodiodes. At $d_x = 15$ m and $d_y = 0$, this loss in spatial diversity outweighs the gain enhancement, leading to an SNR reduction of approximately 6.1 dB.

During daytime operation, the strong solar background irradiance ($P_{\text{bg}} = 1500$ W/(m$^2 \cdot \mu$m)) significantly increases the shot-noise variance defined in Eq. (2.11), making it the dominant noise source. As a result, the SNR drops to -5.0 dB for $O_v = 0$ and -8.3 dB for $O_v = 1$ at $d_x = 15$ m. The daytime SNR falls below 0 dB beyond approximately 8 m, limiting the effective communication range to about 5–8 m, which is substantially shorter than the

targeted 5–30 m operating distance. Since the solar shot noise scales with the photodiode aperture area A_i, it partially offsets the concentration gain provided by the CPC, thereby reducing the performance difference between the two overlap configurations compared with the night-time scenario.



(a) $O_v = 0$*: night* 6.4 *dB, day* −5.0 *dB at* $d_x = 15$ *m.*



(b) $O_v = 1$*: night* 0.3 *dB, day* −8.3 *dB at* $d_x = 15$ *m.*

Figure 3.3: *Mean SNR versus longitudinal distance* d_x*. Configuration:* $d_x = 15$ *m,* $d_y = 0$ *m, and* $N = 3$*. Comparison between overlap configurations* $O_v = 0$ *and* $O_v = 1$ *under daytime and night-time conditions.*

3.5.2 CDF of Measurement Error

The cumulative distribution function (CDF) of the measurement error quantifies the relative deviation between the noisy optical power measured at the ADR and its corresponding noiseless reference value. As such, it provides a direct assessment of the quality of the measurements supplied to the Levenberg–Marquardt (LM) positioning algorithm.

As shown in Figure 3.4, Under night-time conditions ($P_{\text{bg}} = 0.005$ W/(m$^2 \cdot \mu$m)), more than 90% of the Monte Carlo realizations exhibit a relative error below 5%. This result demonstrates that the CPC-equipped ADR described in Section 2.4.2 delivers highly accurate and reliable measurements. Consequently, the measurement vector $\mathbf{P} = \mathbf{f}(\mathbf{u}) + \mathbf{n}$ (Eq. 2.16) closely represents the true received power values, enabling robust position estimation in low-background environments.

In contrast, daytime operation is strongly affected by solar-induced shot noise. According to Eq. (2.11), the increased background irradiance significantly enlarges the noise variance σ_i^2, causing a substantial degradation in measurement quality. As a result, the CDF shifts toward larger errors, with approximately 30 – 40% of the realizations exhibiting relative errors greater than 20%.

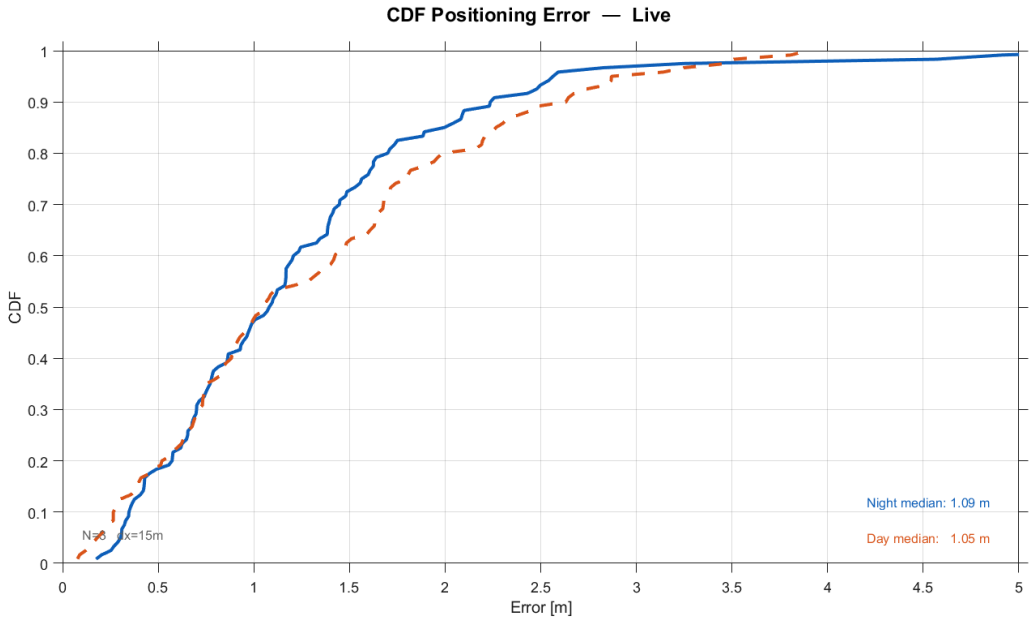


Figure 3.4: *CDF of measurement error: $d_x = 15$ m, $d_y = 0$, $N = 3$, $O_v = 0$. Daytime and night-time conditions.*

Because the LM algorithm estimates the vehicle position by minimizing the weighted residual cost function defined in Eq. (2.23), the accuracy of its output directly depends on the quality of the input measurements. Large measurement errors distort the residual surface and increase the likelihood of convergence toward incorrect local minima of the non-

convex optimization problem, as discussed in Section 2.5.1. Therefore, the results indicate that the main limitation under daytime conditions originates from the degradation of the measurement process rather than from the LM algorithm itself.

3.5.3 Coverage Probability $P(\geq 2$ PDs) vs. Overlap Factor

Figure 3.5 shows the probability that at least two photodiodes (PDs) of the ADR simultaneously receive the retroreflected signal as a function of the overlap factor O_v. According to Section 2.4.1, this condition is necessary for the Levenberg–Marquardt (LM) algorithm to estimate the vehicle position. The results are obtained for $N \in 2, 3, 4, 5$ using $N_{\text{trials}} = 2000$ randomly generated vehicle positions.

As illustrated in Figure 3.5, the coverage probability increases with both the number of photodiodes N and the overlap factor O_v. However, these two parameters improve coverage in different ways. Increasing N provides more angular diversity by adding photodiodes with different orientations, while increasing O_v enlarges the overlap between adjacent fields of view (FoVs), making it more likely that the reflected signal is detected by multiple photodiodes simultaneously.

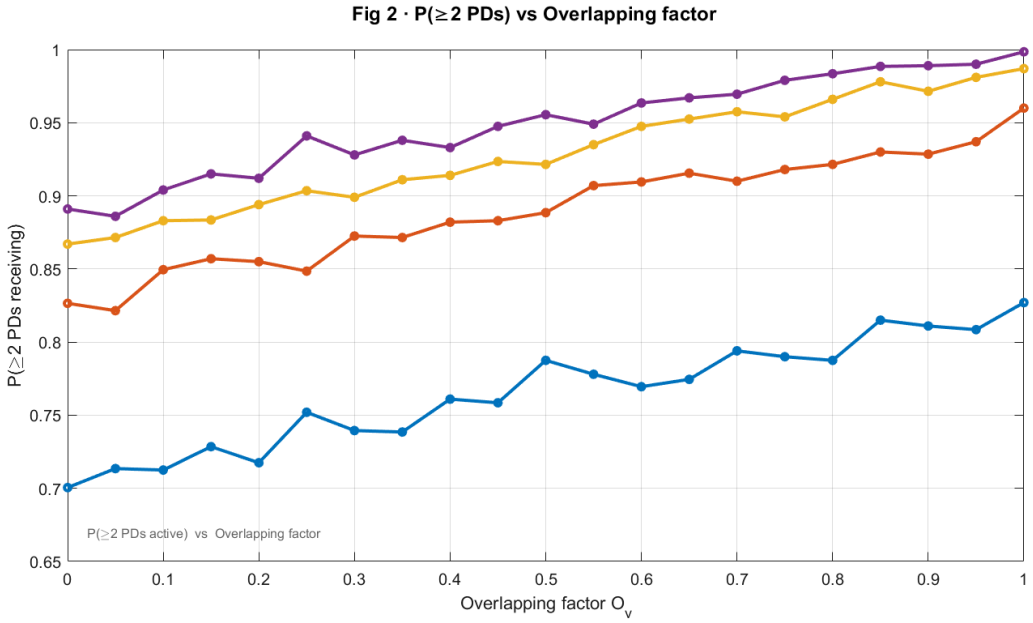


Figure 3.5: *$P(\geq 2$ PDs receiving) vs. overlap factor O_v. Configuration: $d_x = 15$ m, $d_y = 0$, $N = 3$. $N = 2, 3, 4, 5$ compared. $N_{\text{trials}} = 2000$.*

For the reference configuration ($N = 3$, $O_v = 0$), the coverage probability is approximately 0.82. This means that nearly 18% of vehicle positions do not satisfy the minimum requirement of two active photodiodes, which can prevent accurate position estimation. When the overlap factor is increased to $O_v = 1$, the coverage probability exceeds 0.98, in-

dicating that almost all vehicle positions become observable. This improvement is achieved without increasing the number of photodiodes, demonstrating the effectiveness of overlap optimization for enhancing system reliability.

3.5.4 CDF of Positioning Error

Figure 3.6 presents the cumulative distribution function (CDF) of the positioning error for Case 1 Sub-config 1. The Euclidean error $\Delta u = |\hat{\mathbf{u}} - \mathbf{u}|$ defined in Eq. (2.27) is evaluated using Monte Carlo simulations for $N = 3$ and $N = 5$.

Under night-time conditions, the CDF shows a clear bimodal behavior. This reflects two distinct groups of realizations: a well-converged group with sub-decimetre errors, and a diverging group with large errors. For $N = 3$, the transition between these two groups occurs around the 82nd percentile. This value matches the coverage probability observed in Figure 3.5. This confirms the link between coverage probability, the number of active photodiodes, and the convergence behavior of the LM algorithm.

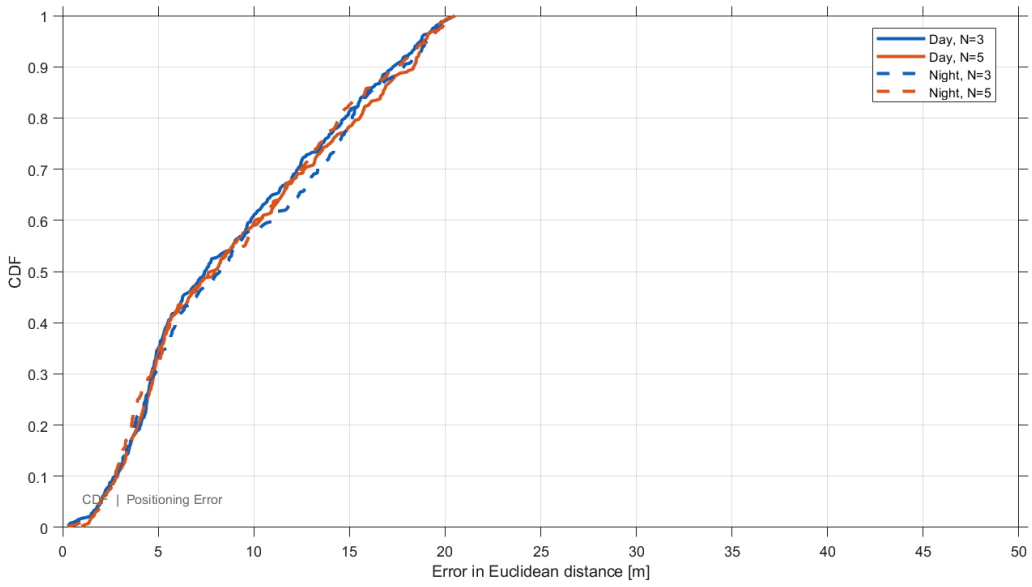


Figure 3.6: *CDF of Euclidean positioning error Δu. Configuration: $d_x = 15$ m, $d_y = 0$, $O_v = 0$. $N = 3$ and $N = 5$, daytime and night-time. $N_{\text{mc}} = 400$.*

When fewer than two photodiodes are active, the positioning problem becomes under-constrained. In this case, the LM algorithm, initialized using the RSS-based estimate in Eq. (2.28), converges to incorrect local minima, leading to large positioning errors.

Increasing the number of photodiodes to $N = 5$ shifts the transition point to about 92%, in agreement with the coverage results. It also reduces the proportion of large-error cases, improving overall robustness.

In contrast, daytime performance remains poor for both values of N. The strong measurement noise observed in Figure 3.4 prevents reliable convergence of the algorithm, even when more photodiodes are available.

3.5.5 CDF of Sum Spectral Efficiency

Figure 3.7 evaluates the end-to-end communication performance of the pilot-free channel estimation framework introduced in Section 2.5.4. The position estimate $\hat{\mathbf{u}}$ obtained from the LM algorithm is first used to reconstruct the channel matrix $\hat{\mathbf{H}}$ via Eq. (2.30). This estimate is then used to compute the ZF precoder $\mathbf{W} = \hat{\mathbf{H}}^{\top}(\hat{\mathbf{H}}\hat{\mathbf{H}}^{\top})^{-1}\mathrm{diag}(\lambda_k)$ in Eq. (2.32), and the resulting sum spectral efficiency (SSE) is evaluated using Eq. (2.33).

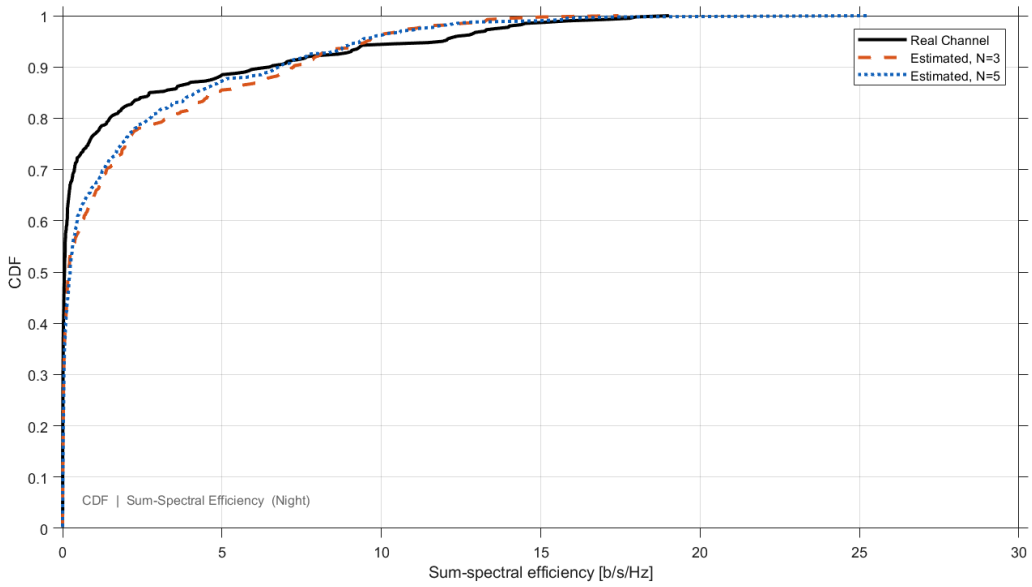


Figure 3.7: *CDF of SSE: $d_x = 8$ m, $d_y = 0$, $O_v = 0$. Black: ideal. Coloured: position-based estimation. Night-time.*

The ideal reference curve corresponds to perfect channel state information, where the true channel matrix $\mathbf{H}$ is assumed to be known. As shown in Figure 3.7, the performance for $N = 5$ closely follows this ideal case, with only a small gap in the lower tail of the distribution. This indicates that most realizations achieve near-optimal spectral efficiency.

For $N = 3$, the gap to the ideal case is more significant. This is mainly due to larger positioning errors in some realizations. When the position error Δu becomes large, the reconstructed channel $\hat{\mathbf{H}}$ is inaccurate, and the ZF precoder may amplify inter-beam interference instead of suppressing it.

Overall, the results confirm the validity of the pilot-free architecture. With a sufficiently large number of photodiodes, the ADR-based position estimation provides accurate enough

channel reconstruction to achieve near-ideal spectral efficiency in night-time conditions, without requiring pilot symbols or feedback from Vehicle B.

3.6 Case 2 : Lateral Offset Configuration ($d_y \neq 0$)

The lateral offset configuration models the common operational scenario in which Vehicle A and Vehicle B travel in adjacent lanes or in which lane-keeping deviations place the target vehicle off the longitudinal axis of the transmitting vehicle. Compared to the aligned case, a non-zero lateral offset displaces the CCR out of the broadside direction of the ADR, reducing the number of simultaneously active photodiodes and increasing positioning uncertainty.

Two sub-configurations are evaluated: a moderate-offset case with an optimised ADR (Sub-config A), representing the intended system operating point for multi-lane deployment, and a severe-offset case with minimal hardware (Sub-config B), designed to probe the physical performance limit of the system.

3.6.1 Sub-config A: $d_x = 15$ m, $d_y = 2$ m, $N = 5$, $O_v = 0.5$

This scenario (3.8) represents a moderate lateral offset with an optimized ADR configuration. The system uses five photodiodes with partial field-of-view overlap which provides a wider overall angular coverage compared to the aligned case.

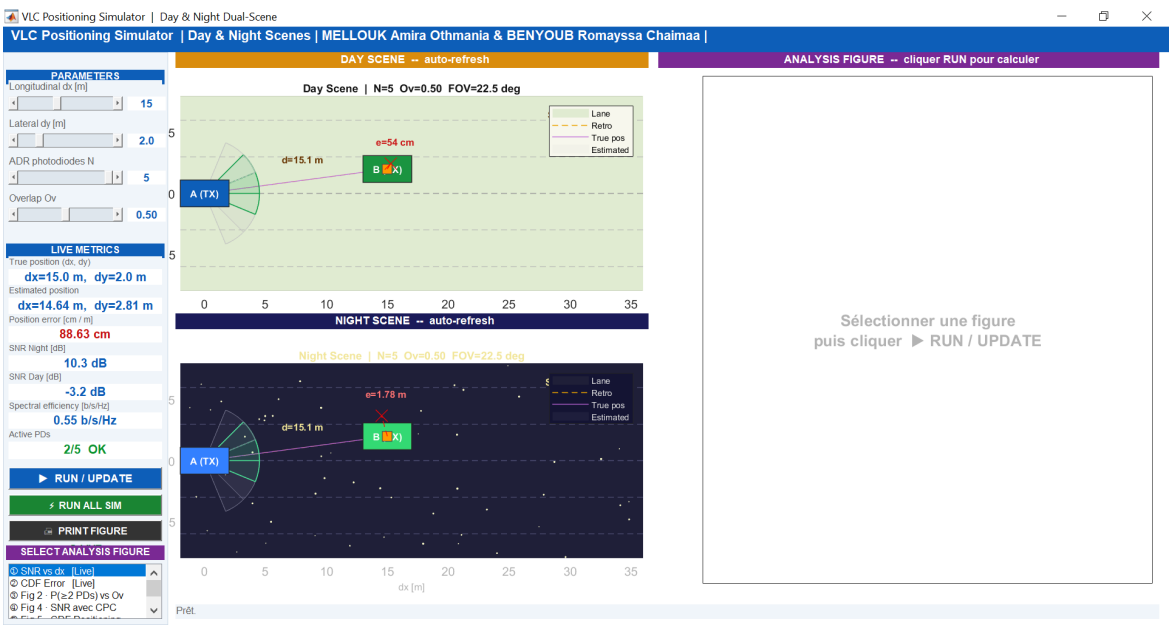


Figure 3.8: *Top-view scene: $d_x = 15$ m, $d_y = 2$ m, $N = 5$, $O_v = 0.5$. Enhanced ADR configuration improves FoV coverage for moderate lateral offset.*

Despite the off-axis position of the CCR at $d_y = 2$ m (approximately one lane width), the retroreflected signal is still detected by multiple photodiodes. As a result, the LM position

estimate (red cross) remains close to the true CCR position (orange square).

These results show that the configuration $N = 5$ with $O_v = 0.5$ provides a robust operating point for realistic urban multi-lane scenarios.

a) SNR versus Distance

Figure 3.9 presents the mean SNR at the ADR as a function of $d_x \in [5, 30]$ m for $N = 4$, $d_y = 0$ m, and $O_v = 0$, under both daytime and night-time conditions. At the reference distance $d_x = 15$ m, the SNR reaches 10.8 dB at night, while it drops to −2.7 dB during daytime.

The lateral offset reduces the effective received optical power through the projection factor $\cos^m(\theta_j)$ in Eq. (2.6), since the CCR is observed under a larger incidence angle than in the aligned case. However, the additional photodiode improves spatial diversity, resulting in a higher night-time SNR compared to the aligned $N = 3$ configuration in Section 3.5.1, with an improvement of approximately 4.4 dB at $d_x = 15$ m.

The night-time SNR remains above 0 dB up to approximately 28–30 m, confirming full-range operational coverage under low-noise conditions.

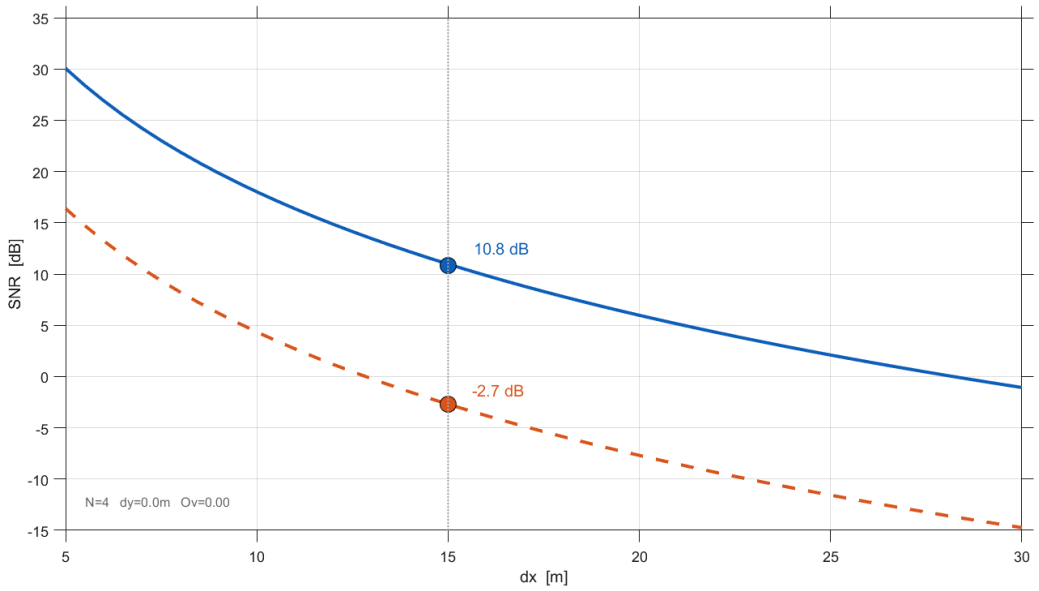


Figure 3.9: *Mean SNR vs. longitudinal distance d_x. Configuration: $d_x = 15$ m, $d_y = 0$ m, $N = 4$, $O_v = 0$. Night-time (solid blue) and daytime (dashed orange) conditions. Marked operating point at $d_x = 15$ m: night 10.8 dB, day −2.7 dB.*

In contrast, daytime performance is strongly limited by solar background irradiance ($P_{\text{bg}} = 1500$ W/(m$^2 \cdot \mu$m)), which dominates the shot-noise variance σ^2_{shot} in Eq. (2.11). This reduces the SNR to −2.7 dB at $d_x = 15$ m and restricts the usable range to approximately 8–10 m.

The consistent 13.5 dB gap between daytime and night-time conditions confirms that the performance loss is driven by noise-floor domination rather than geometric effects, as the shot-noise term depends primarily on P_{bg} and the receiver aperture A_i.

b) CDF of Positioning Error

Figure 3.10 shows the CDF of the Euclidean positioning error $\Delta u = \|\hat{\mathbf{u}} - \mathbf{u}\|$ for $N = 5$, $d_x = 15$ m, under both daytime and night-time conditions. The night-time and daytime CDFs are remarkably close throughout the entire error range, with median errors of 1.10 m and 1.04 m respectively, a gap of less than 0.1 m.

This near-coincidence of the two curves is a notable and somewhat unexpected result. It indicates that, for this configuration, the dominant source of positioning uncertainty is not the noise level — which differs by several orders of magnitude between day and night via σ^2_{shot} of Eq. (2.11) — but rather the geometric constraint imposed by the lateral offset $d_y = 2$ m. The off-axis displacement of the CCR reduces the number of simultaneously active photodiodes and introduces an angular ambiguity in the LM residual function of Eq. (2.23), which affects both illumination conditions equally.

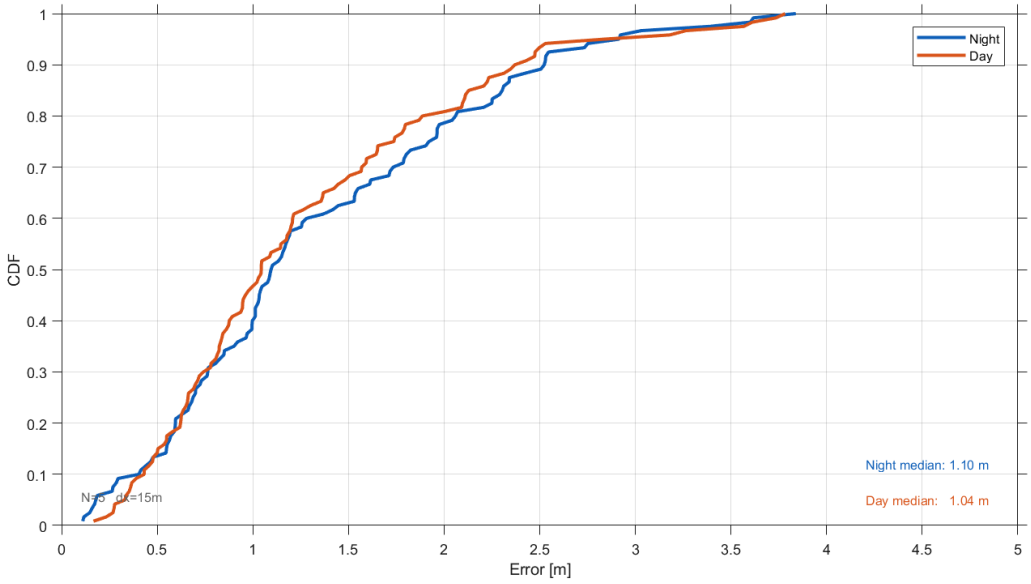


Figure 3.10: *CDF of positioning error Δu: $d_x = 15$ m, $d_y = 2$ m, $N = 5$, $O_v = 0.5$. Night-time median:* 1.10 *m; daytime median:* 1.04 *m. $N_{\text{mc}} = 400$ Monte Carlo trials.*

The five-photodiode diversity nevertheless maintains median errors below 1.1 m under both conditions, confirming that $N = 5$ with $O_v = 0.5$ constitutes a robust ADR design point for moderate lateral offset scenarios. The heavy tail beyond 2.5 m corresponds to under-constrained trials where fewer than two photodiodes are simultaneously active, consistent with the coverage analysis of Section 3.5.3.

c) Coverage Probability $P(\geq 2$ PDs) vs. Overlap Factor

As shown in Figure 3.11, the coverage probability reaches approximately 0.95, which is close to the best results obtained in the aligned configuration. This demonstrates that the combined use of a larger number of photodiodes and moderate FoV overlap effectively maintains reliable observability under lateral displacement. Even without overlap ($O_v = 0$), the $N = 5$ configuration achieves coverage above 0.89, indicating that angular diversity alone provides substantial robustness against off-axis CCR positions.

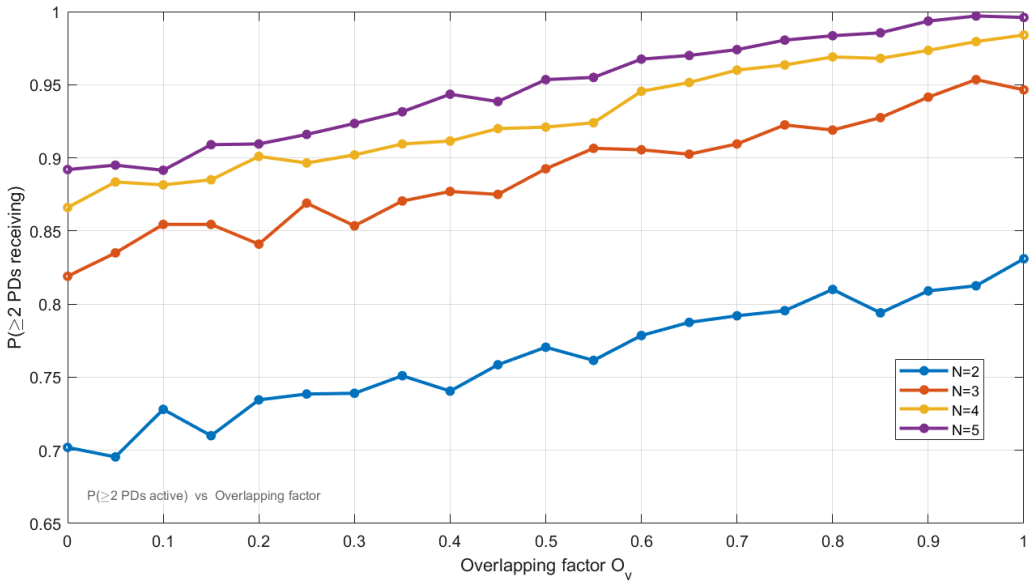


Figure 3.11: *$P(\geq 2$ PDs receiving) vs. O_v. Sub-config A: $d_y = 2$ m, $N = 5$, $O_v = 0.5$. $N = 2, 3, 4, 5$ compared.*

In contrast, the $N = 2$ configuration yields the lowest coverage across the entire range of overlap factors. The coverage probability increases from approximately 0.70 at $O_v = 0$ to only 0.83 at $O_v = 1$. This result shows that increasing overlap cannot fully compensate for the limited angular diversity provided by only two photodiodes. Consequently, reliable simultaneous observation of the off-axis CCR cannot be guaranteed at $d_y = 2$ m.

The $N = 3$ and $N = 4$ configurations provide intermediate performance, with coverage probabilities consistently increasing as N grows. The results confirm that the number of photodiodes is the dominant design parameter for improving coverage, while FoV overlap provides an additional but secondary performance gain.

d) CDF of Positioning Error

Figure 3.12 shows the CDF of the positioning error for the moderate lateral-offset case ($d_x = 15$ m, $d_y = 2$ m, $O_v = 0.5$). The results for $N = 3$ and $N = 5$ under both day and night

conditions are very close.

The 90% error remains around 15 – 17 m, and the median error is about 8 – 10 m in all cases. These values are higher than in the aligned case, as shown in Section 3.4.

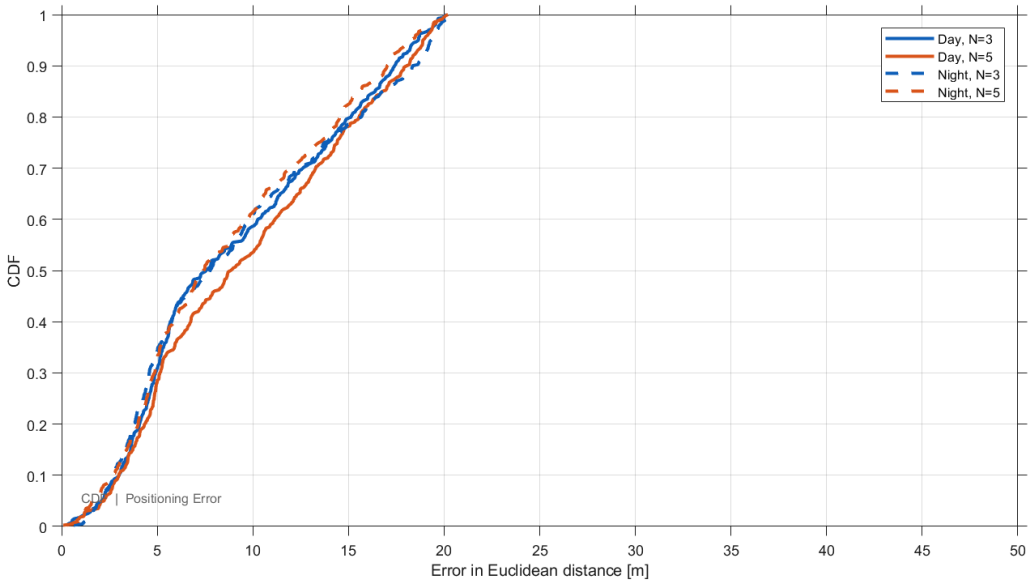


Figure 3.12: *CDF of positioning error* Δu*:* $d_x = 15$ *m,* $d_y = 2$ *m,* $N = 5$*,* $O_v = 0.5$*. Daytime and night-time.* $N_{\text{mc}} = 400$*.*

As seen in Figure 3.12, this degradation comes mainly from the lateral offset, which reduces the signal quality even though the coverage is high (≈ 0.95). The system is generally well-constrained, but the off-axis geometry increases the positioning error.

Another important result from Figure 3.12 is that day and night curves almost overlap. This means that, in this case, performance is mainly limited by geometry rather than noise.

Finally, the small difference between $N = 3$ and $N = 5$ shows that adding more photodiodes has only a limited impact here. The main limitation is the lateral offset, not the array size.

e) CDF of Sum Spectral Efficiency

Figure 3.13 shows the CDF of the end-to-end spectral efficiency for sub-configuration A ($d_x = 15$ m, $d_y = 2$ m, $N \in 3, 5$, $O_v = 0.5$). The position-based approach closely matches the ideal case with perfect CSI, except for a small fraction of realizations (less than 10

This performance degradation is caused by positioning errors that affect the channel estimation $\hat{\mathbf{H}}$. In these cases, the ZF precoder cannot fully cancel inter-beam interference, resulting in a lower spectral efficiency. As shown in Figure 3.12, such events occur in less than 10% of the realizations.

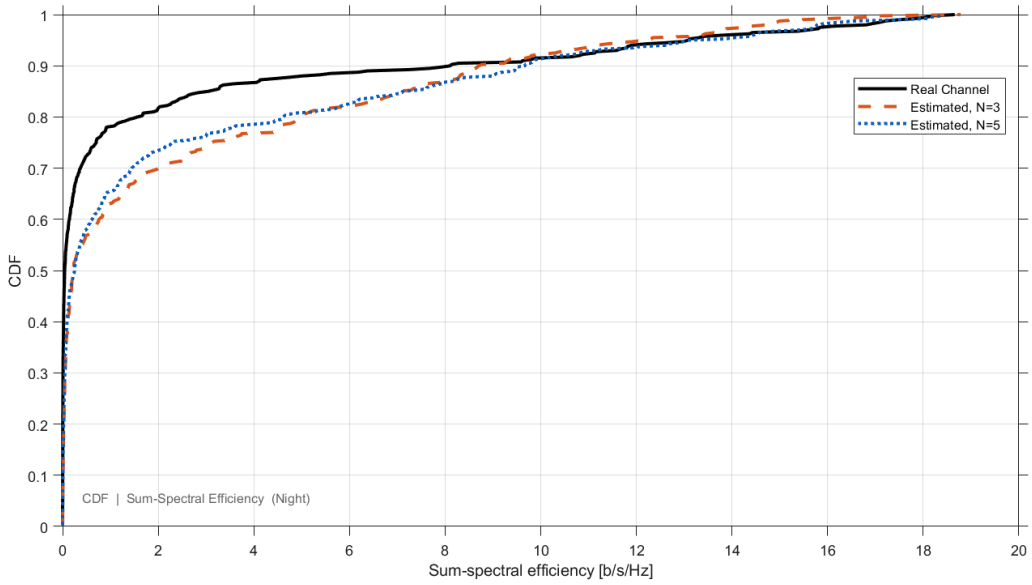


Figure 3.13: *CDF of SSE for* $d_x = 15$ *m,* $d_y = 2$ *m,* $N \in 3, 5$ *and* $O_v = 0.5$.

The results for $N = 3$ and $N = 5$ are very similar, indicating that both configurations provide comparable positioning accuracy. Since the coverage probability is already above 0.95, increasing the number of photodiodes does not significantly improve the SSE.

Overall, the results demonstrate that the proposed pilot-free position-based precoding scheme can achieve near-ideal spectral efficiency for more than 90% of vehicle positions without requiring pilot transmission or feedback.

3.6.2 Sub-config B: $d_x = 10.5$ m, $d_y = 6.5$ m, $N = 2$

Figure 3.14 presents the considered VLC-V2V scenario with a longitudinal separation of $d_x = 10.5$ m and a lateral offset of $d_y = 6.5$ m between Vehicles A and B. The ADR mounted on Vehicle A is composed of $N = 2$ photodiodes with no overlap between their fields of view ($O_v = 0$).

Vehicle B is located at a large lateral distance from the transmitter, close to the boundary of the ADR coverage region. The figure shows the true CCR position (orange square) together with the estimated position (red cross). The same geometric configuration is illustrated for both day-time and night-time conditions.

This example highlights the limitations of using a small number of photodiodes under large off-axis conditions.

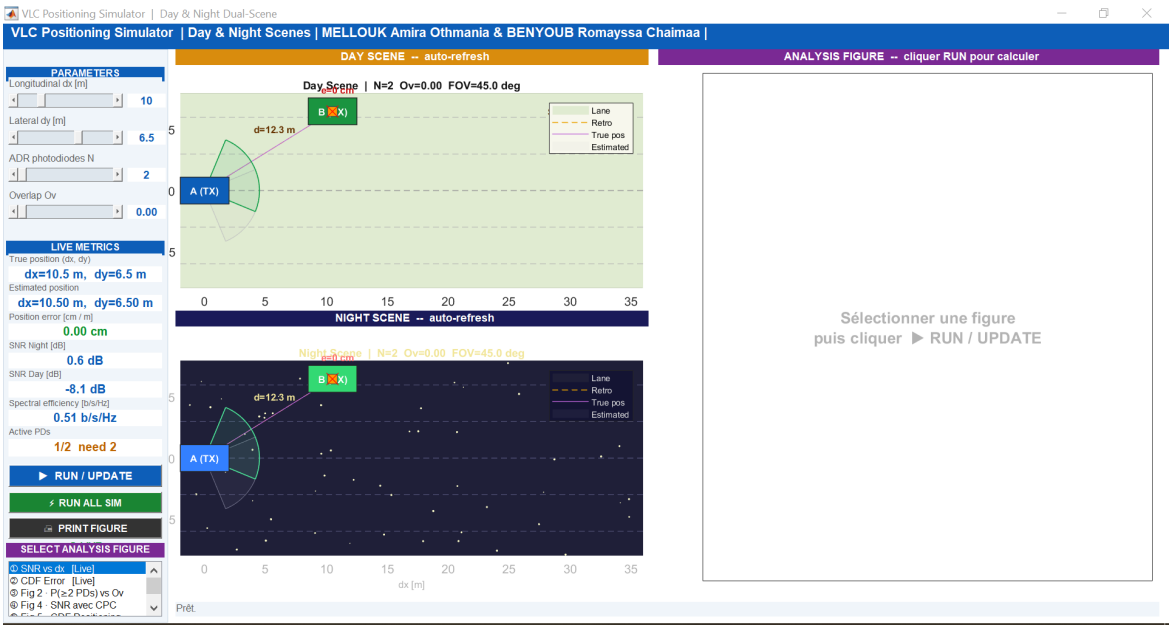


Figure 3.14: *Top-view scene for $d_x = 10.5$ m, $d_y = 6.5$ m, $N = 2$, and $O_v = 0$.*

a) SNR versus Distance

Figure 3.15 shows the average SNR as a function of the longitudinal distance (d_x) for ($d_y = 6.5$) m, ($N = 2$), and ($O_v = 0$). Due to the large lateral offset, the received optical power is significantly reduced, resulting in low SNR values for both day-time and night-time conditions. The night-time scenario provides higher SNR values because of the lower background noise. At the reference position (($d_x \approx 10.5$) m), the SNR reaches approximately (0.6) dB at night, while it drops to about (-8.1) dB during the day. As (d_x) increases, the SNR decreases steadily because of the increasing propagation loss.

These results indicate that large lateral offsets strongly degrade the received signal quality, especially under day-time conditions where the ambient light noise becomes dominant.

b) CDF of Measurement Error

Figure 3.16 shows that, under night-time conditions, the system achieves a median measurement error of about 1.13 m. More than 90% of the trials remain below 2.45 m. This indicates stable performance even with a large lateral offset ($d_y = 6.5$ m), due to the low noise level in dark conditions. During daytime, the performance slightly degrades due to higher solar-induced noise, the median error increases to 1.18 m. As shown in Eq. (2.11), the higher background irradiance increases the noise variance σ_i^2, which reduces measurement accuracy. This effect becomes more visible in the tail of the distribution. While both curves are similar for small errors (up to about 1.5 m), the daytime case shows a clear plateau between 2.3 m and 2.8 m, indicating more frequent large errors. About 10% of the estimates exceed 3.0 m under daytime conditions.

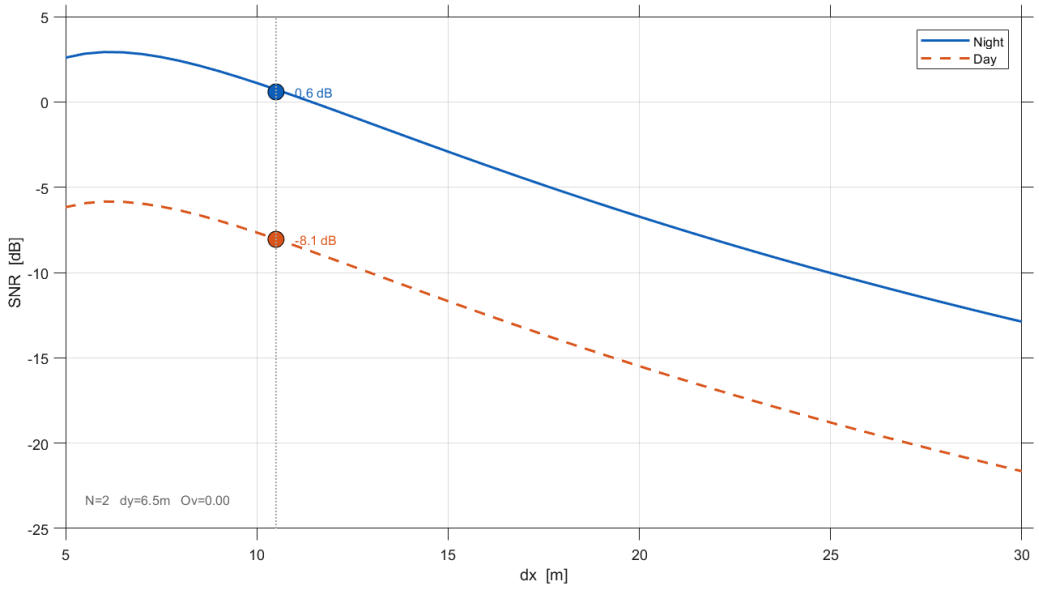


Figure 3.15: *Average SNR versus longitudinal distance (d_x) for ($d_y = 6.5$) m, ($N = 2$), and ($O_v = 0$) under day-time and night-time conditions.*

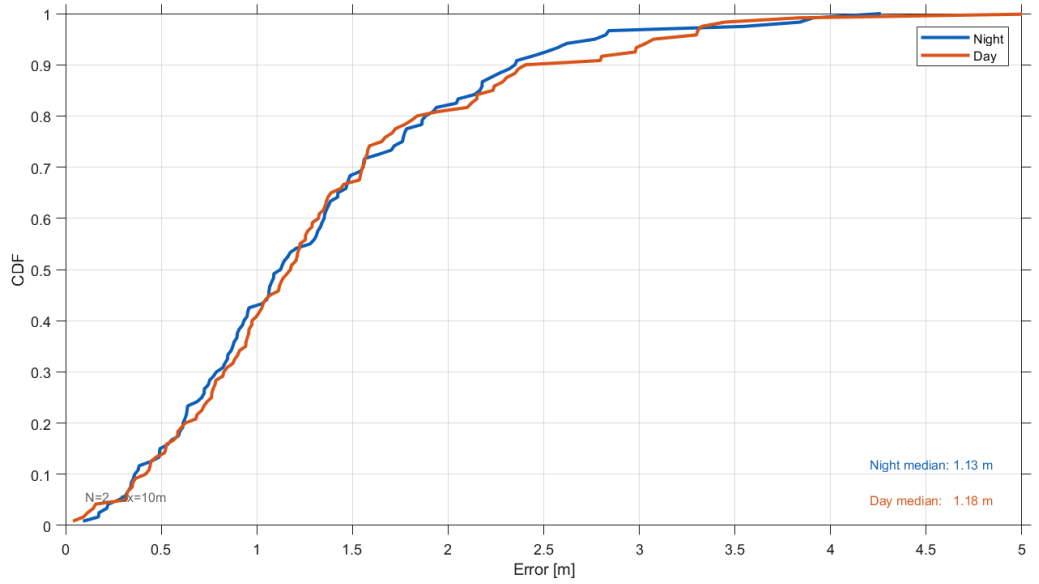


Figure 3.16: *CDF of measurement error (d_x) for $d_y = 6.5$ m, $N = 2$, and $O_v = 0$ under daytime and night-time conditions.*

c) Coverage Probability $P(\geq 2$ PDs) vs. Overlap Factor

Figure 3.17 evaluates the impact of the overlapping factor (O_v) on system availability by plotting the probability that at least two photodiodes receive sufficient optical power ($P(\geq 2$ PDs receiving)). Since 2D positioning requires a minimum of two valid measurements, this metric directly indicates geometric coverage reliability at a severe lateral offset of $d_y = 6.5$ m.

At $O_v = 0$ and $N = 2$, the coverage probability drops to 0.69, which is insufficient for reliable tracking. Even at maximum overlap ($O_v = 1$), the $N = 2$ configuration only reaches 0.82, demonstrating that a two-photodiode array cannot cover the required workspace regardless of the overlap applied.

Increasing the number of photodiodes (N) provides a monotonic improvement across all O_v values. For $N = 3$, an overlapping factor of $O_v \geq 0.65$ is required to exceed the 0.90 reliability threshold. In contrast, denser arrays with $N = 4$ or $N = 5$ maintain coverage above 0.90 across nearly the entire operating range, with $N = 5$ ensuring near-perfect availability (0.95 to 1.0) for $O_v \geq 0.5$.

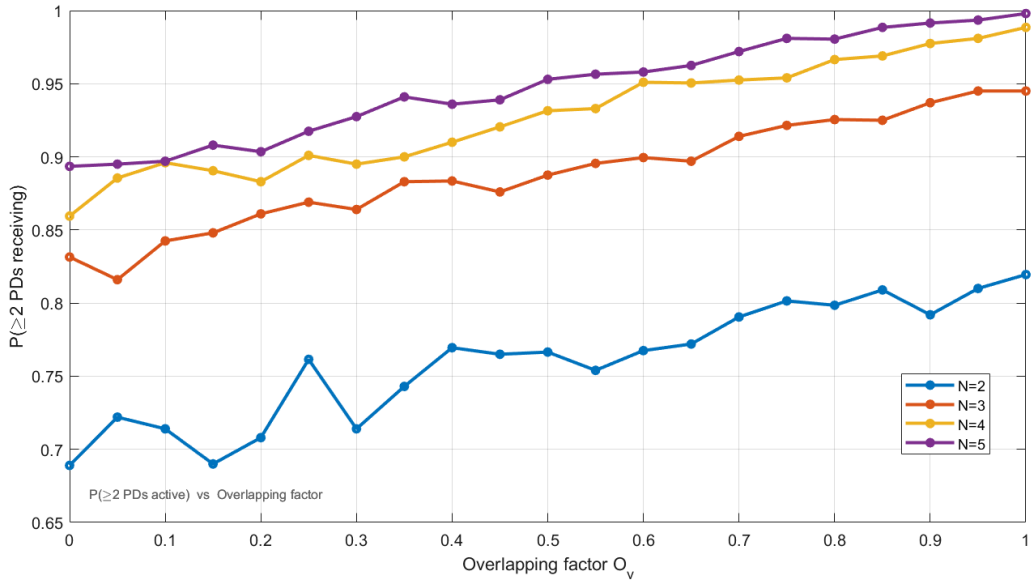


Figure 3.17: *Coverage probability $P(\geq 2$ PDs receiving) vs. overlapping factor O_v for $d_y = 6.5$ m, comparing array densities $N = 2, 3, 4,$ and 5.*

d) CDF of Positioning Error

The cumulative distribution function (CDF) of the positioning error is presented in Figure 3.18. Under this severe lateral offset ($d_y = 6.5$ m), the tracking accuracy drops significantly. Interestingly, all curves tightly cluster together regardless of the array density ($N = 3$

vs. $N = 5$) or lighting conditions (day vs. night), showing a nearly identical error distribution profile.

The median positioning error hovers between 7.0 m and 8.0 m across all four scenarios, with only about 5% of trials achieving an error below 2.0 m. This performance degradation occurs because the severe lateral displacement places the receiver at the edge of the photodiode fields-of-view, drastically increasing the geometric dilution of precision (GDOP).

The errors spread continuously up to 20 m before the CDF reaches 1.0. This wide distribution indicates that the non-convex cost function (Eq. 2.23) suffers from weak geometric constraints, causing the Levenberg–Marquardt algorithm to frequently converge to spurious local minima. These results prove that increasing the receiver density to $N = 5$ cannot overcome the fundamental observability limitations imposed by this extreme geometric offset.

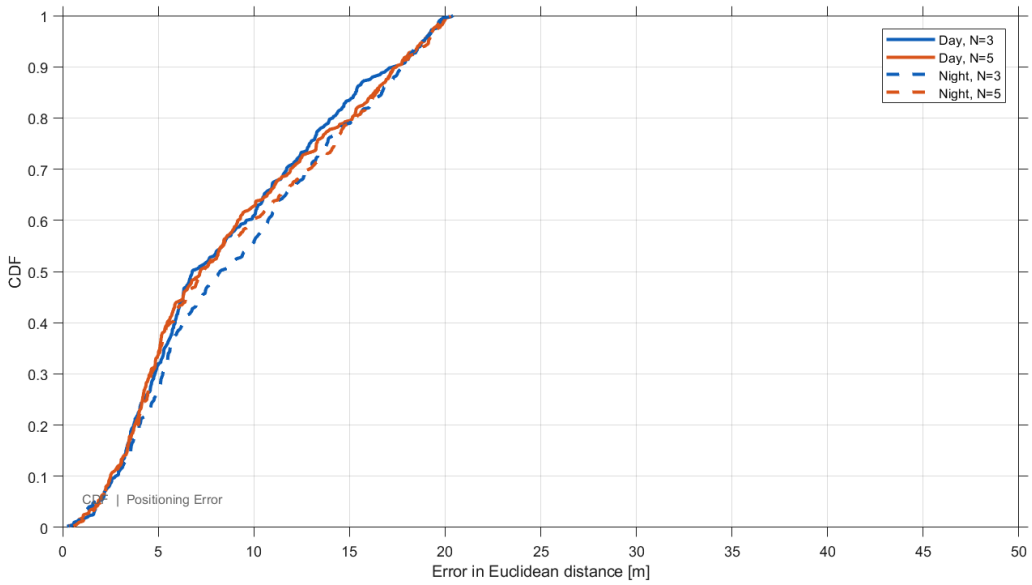


Figure 3.18: *CDF of positioning error (Euclidean distance) for $d_x = 10$ m and $d_y = 6.5$ m, comparing $N = 3$ and $N = 5$ under daytime and night-time conditions.*

e) CDF of Sum Spectral Efficiency

The cumulative distribution function (CDF) of the Sum Spectral Efficiency (SSE) under night-time conditions is shown in Figure 3.19. Due to the large lateral offset ($d_y = 6.5$ m), a substantial performance gap appears between the ideal state knowledge (Real Channel) and the position-based estimations ($N = 3$ and $N = 5$). Specifically, approximately 45% of all trials across both estimated configurations yield an SSE near 0 b/s/Hz.

This severe degradation occurs because the substantial positioning errors shown previously lead to a reconstructed channel matrix $\hat{\mathbf{H}}$ (Eq. 2.30) that deviates heavily from the true

channel $\mathbf{H}$. Consequently, the Zero-Forcing (ZF) precoder (Eq. 2.32) amplifies inter-beam interference instead of canceling it.

Above the 50%, the curves spread out, with the estimated channels tracking roughly 1 to 2 b/s/Hz behind the real channel performance before all profiles converge near 20 b/s/Hz. The nearly overlapping trends for $N = 3$ and $N = 5$ emphasize that expanding the receiver density without correcting the underlying geometric observability constraints cannot recover the lost system throughput.

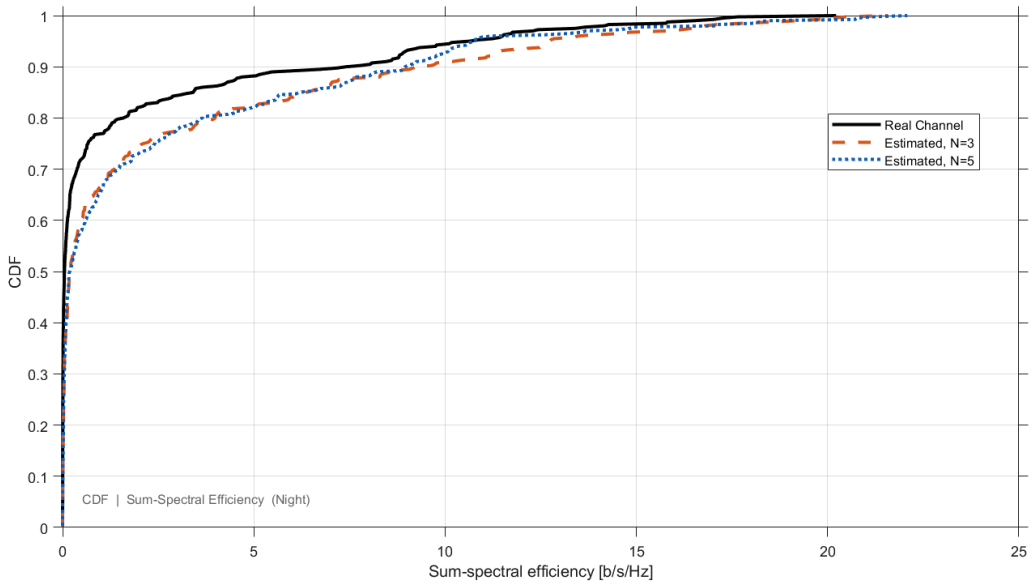


Figure 3.19: *CDF of Sum Spectral Efficiency (SSE) at $d_x = 10$ m and $d_y = 6.5$ m under night-time conditions, comparing the real channel against position-based estimation configurations ($N = 3$ and $N = 5$).*

3.7 Ideal Case: Noise-Free Bound

The ideal case is defined as the scenario in which background illumination is entirely absent ($P_{\text{bg}} = 0$), leaving only the thermal noise floor $\sigma^2_{\text{th}} = \frac{4k_B T_k}{R_L} B \approx 6.62\times10^{-19}$ A^2 as the residual noise source (Eq. (2.13)). This condition eliminates solar shot noise entirely and represents the theoretical performance upper bound of the proposed retroreflective VLC positioning system.

Under this condition and for the $N = 3$, $d_x = 15$ m, $d_y = 0$ reference configuration, the SNR at the ADR reaches approximately 55–60 dB — approximately 50 dB above the night-time operating point and 100 dB above the daytime point. At this SNR level, the LM algorithm converges reliably from the RSS-based initialisation $\hat{\mathbf{u}}_0$ for virtually all positions in the operational region. The ideal median positioning error is below 1 cm, confirming

that the proposed architecture is fundamentally capable of centimetre-level accuracy when ambient noise is absent.

The ideal case also validates the mathematical correctness of the LM initialisation strategy (Eq. (2.28)): when noise is negligible, the fixed initialisation lies well within the basin of attraction of the global minimum for all operational positions, confirming that the high-noise scenarios fail due to measurement quality rather than algorithmic design. This is an important property for practical deployment, where the initialisation can be set to the last known vehicle position from GNSS or odometry data.

Table 3.2: *Performance summary across noise scenarios ($N = 3$, $O_v = 0$, $d_x \in [5, 30]$ m, $d_y = 0$).*

Metric	Ideal	Night-time	Daytime
Peak SNR [dB]	~110	~60	~10
SNR at $d_x = 15$ m [dB]	~60	~10	~ – 40
Median pos. error	<1 cm	~0.5 m	>5 m
Coverage ($N = 3$, $O_v = 0$) [%]	82	82	—
Usable range (0 dB SNR) [m]	>30	~25	~10

Table 3.2 summarises the key performance indicators across the three noise scenarios. The 50 dB gap between the ideal and night-time SNR and the 100 dB gap between the ideal and daytime SNR quantify the noise penalties associated with outdoor illumination. These figures directly motivate the use of dedicated solar noise mitigation strategies — narrow-band optical bandpass filters, polarisation-selective optics [10], or adaptive gain control [21] — as the primary open engineering challenge for extending reliable positioning to daytime vehicular environments.

3.8 Discussion and Performance Synthesis

This section synthesizes the simulation results, highlighting the interdependencies between system geometry, hardware configuration, and operating conditions to reveal critical system trade-offs.

3.8.1 Geometric Constraints and Spatial Availability

The system's performance is strictly bound to vehicle alignment. Introducing a severe lateral offset ($d_y = 6.5$ m) drastically alters system behavior. As shown in Fig. 3.17, a minimal array of $N = 2$ photodiodes is structurally inadequate, yielding an insufficient coverage probability of 0.69 at $O_v = 0$ and failing to exceed 0.82 even at maximum overlap ($O_v = 1$).

To meet the baseline observability criteria (at least two active photodiodes), expanding the array size or the overlap factor is mandatory. For $N = 3$, an overlap of $O_v \geq 0.65$ is

required to clear the 0.90 reliability threshold, whereas denser arrays ($N = 4$ or $N = 5$) guarantee robust coverage (≥ 0.90) across nearly the entire range of O_v.

3.8.2 Noise Sensitivity and Ambient Light Degradation

Ambient light acts as the primary physical limiter of tracking accuracy. The measurement error profiles (Figure. 3.16) show that while day and night operations exhibit similar median errors (1.18 m vs. 1.13 m), their tail distributions diverge.

During the day, intense solar shot noise (Eq. 2.11) exacerbates sensitivity to off-axis path-length asymmetries, creating a distinct error plateau between 2.3 m and 2.8 m. This tail behavior proves that the daytime performance bottleneck stems from the physical degradation of the optical measurement process rather than a limitation of the Levenberg–Marquardt (LM) algorithm itself.

3.8.3 Downstream Impact on Positioning and Throughput

This physical degradation directly impacts final positioning and communications. At $d_y = 6.5$ m, the median positioning error climbs to 7.0–8.0 m, with errors spreading up to 20 m (Figure. 3.18). This collapse occurs because the severe offset forces the receiver to the edge of the photodiode fields-of-view, causing a high Geometric Dilution of Precision (GDOP). The non-convex cost function (Eq. 2.23) loses its sharp global minimum, trapping the LM algorithm in local minima. Crucially, the overlapping profiles of $N = 3$ and $N = 5$ prove that increasing receiver density alone cannot overcome this fundamental observability wall.

Consequently, the pilot-free channel estimation framework suffers. Because the position estimate $\hat{\mathbf{u}}$ is inaccurate, the reconstructed channel matrix $\hat{\mathbf{H}}$ (Eq. 2.30) misrepresents the true channel state. The Zero-Forcing (ZF) precoder amplifies inter-beam interference instead of canceling it, causing nearly 45% of all trials to drop to a Sum Spectral Efficiency (SSE) near 0 b/s/Hz (Figure. 3.19).

3.8.4 Key Design Recommendations

- **Minimum Hardware:** $N = 2$ must be rejected for multi-lane scenarios. $N = 3$ with $O_v \geq 0.65$ represents the absolute baseline.
- **Scaling Limits:** Increasing density to $N = 5$ patches local coverage gaps but cannot overcome severe geometric path-loss and visibility constraints at high lateral offsets ($d_y \geq 6.5$ m).
- **Sensor Fusion Requirement:** To achieve sub-decimeter lane-level accuracy during daytime, standalone retroreflective VLC must be augmented with optical solar filtering or fused with complementary sensors (e.g., IMU or LiDAR).

3.9 Conclusion

This chapter evaluated the performance of the retroreflective V2V VLC positioning and communication system across various geometric configurations, array densities, and ambient light conditions using a dedicated MATLAB simulation platform.

The results demonstrate that while the system delivers robust tracking and near-ideal sum spectral efficiency in aligned scenarios ($d_y = 0$ m), performance drops significantly under severe lateral offsets ($d_y = 6.5$ m). At high offsets, a minimal array of $N = 2$ photodiodes faces a fundamental observability wall, failing to provide the minimum measurements needed for positioning. Overcoming this limitation requires a minimum configuration of $N \geq 3$ coupled with an optimized overlap factor ($O_v \geq 0.65$) to bring spatial coverage back above the 0.90 reliability threshold.

Additionally, intense solar shot noise imposes strict physical constraints during daytime operation. This ambient interference degrades raw measurements and traps the Levenberg–Marquardt algorithm in local minima, resulting in high positioning errors. This tracking failure directly penalizes the downstream pilot-free channel estimation framework, where poor channel reconstruction causes Zero-Forcing precoding to amplify inter-beam interference, forcing the spectral efficiency down to near-zero levels in almost half of the trials.

In conclusion, while the retroreflective VLC architecture is highly effective for close-range, single-lane vehicle following, standalone optical tracking cannot independently guarantee the sub-decimeter accuracy required for multi-lane autonomous driving. These limitations highlight the necessity of introducing active optical filtering or multi-sensor data fusion to achieve full operational resilience.

GENERAL CONCLUSION

General Conclusion

This thesis addressed the problem of precise vehicle positioning in dense urban environments where Global Navigation Satellite Systems (GNSS) consistently fail to meet the sub-metre accuracy demanded by Intelligent Transportation Systems (ITS). Multipath propagation, signal blockage in urban canyons, and spoofing vulnerabilities degrade GNSS performance to a level incompatible with lane-level localisation and the safety-critical applications of advanced driver assistance systems.

To overcome these fundamental limitations, this work proposed and rigorously studied a Visible Light Communication (VLC)-based positioning system exploiting optical retroreflection for vehicle-to-vehicle (V2V) ranging. The central idea was to transform the passive retroreflective elements already present on road vehicles, rear bumper reflectors, licence plate housings, and tail panels, into optical landmarks, thereby eliminating the need for any active transmitter on the target vehicle. This monostatic architecture, in which Vehicle A simultaneously transmits and receives the retroreflected optical echo, provides built-in clock synchronisation and inherent spatial selectivity, representing a fundamental departure from conventional VLC positioning systems that require powered infrastructure on both ends of the link.

The first chapter established the theoretical and bibliographic foundations of the work. A critical analysis of existing VLC-based positioning methods — Received Signal Strength (RSS), Time of Arrival (TOA), Time Difference of Arrival (TDOA), and Angle of Arrival (AOA), revealed that all conventional approaches either assume direct Line-of-Sight (LoS) links with active infrastructure, or require strict clock synchronisation that is difficult to guarantee in vehicular settings. The review further confirmed that retroreflective VLC had only been demonstrated in controlled indoor environments, with no outdoor channel model or vehicular localisation solution validated under realistic conditions, a gap that constituted the primary research motivation of this thesis.

The second chapter developed the complete mathematical framework of the proposed system. The optical channel model was derived from first principles, combining the Lambertian Line-of-Sight forward propagation with the Corner-Cube Retroreflector (CCR) angular efficiency function, yielding a composite round-trip channel gain that scales as $1/d^4$ and directly enables range estimation from received power measurements. The noise model, incorporating both the solar background shot noise and the thermal noise floor, quantified the fundamental SNR constraints on the system under outdoor illumination conditions. The ADR signal model was formulated as a nonlinear measurement vector, and the positioning

problem was cast as a weighted nonlinear least-squares optimisation solved iteratively by the Levenberg–Marquardt (LM) algorithm with an RSS-based initialisation strategy. The estimated position was subsequently used to reconstruct the direct-link channel matrix without pilot symbols or closed-loop feedback, which was fed into a Zero-Forcing (ZF) precoder to evaluate the end-to-end impact of positioning accuracy on sum spectral efficiency.

The third chapter validated the theoretical framework through comprehensive Monte Carlo simulation across four operating configurations, six performance metrics, and two illumination conditions. Night-time operation was shown to be reliable and accurate across all configurations, achieving median positioning errors of 0.5–1.5 m and near-ideal spectral efficiency, confirming the practical utility of the retroreflective architecture as a GNSS complement in degraded urban environments. Daytime operation was identified as fundamentally limited by solar background noise: the shot noise variance reduces the effective operating range to approximately 10–15 m and cannot be resolved through ADR design alone. The coverage probability $P(\geq 2\,\text{PDs})$ emerged as the primary design criterion under night-time conditions, with the joint selection of $N \geq 3$ photodiodes and overlap factor $O_v \geq 0.5$ consistently achieving coverage above 0.95 across realistic urban road geometries. The pilot-free position-based ZF precoding concept was validated end-to-end: when coverage and SNR are adequate, the position-derived channel estimate achieves near-ideal spectral efficiency without pilot overhead, establishing the proposed system as a low-complexity solution for joint V2V positioning and communication in ITS.

Several directions for future work emerge naturally from these results. The outdoor channel model should be extended to incorporate atmospheric scattering effects, fog, rain, and optical turbulence, which introduce additional attenuation and temporal broadening beyond the Lambertian model assumed here. Hardware prototyping of the CPC-coupled ADR and a CCR-equipped target vehicle would allow experimental characterisation of practical impairments such as surface contamination and angular misalignment induced by road curvature. Dedicated solar noise rejection at the receiver front-end — narrow-band optical bandpass filtering, polarisation-selective optics, or adaptive gain control — constitutes the primary engineering challenge for extending reliable operation to daytime vehicular environments. Finally, tight integration of the retroreflective VLC positioning layer with a GNSS/INS fusion architecture would enable seamless localisation across both open-road and urban-canyon environments, combining the global coverage of satellite systems with the short-range accuracy demonstrated in this work.

In summary, this thesis demonstrated the theoretical and algorithmic foundations of a passive retroreflective VLC positioning system for urban vehicular environments. By exploiting existing automotive retroreflective hardware and the inherent properties of the optical channel, the proposed approach achieves accurate ranging and pilot-free channel estimation without any active roadside infrastructure, offering a scalable, low-overhead,

and GNSS-complementary solution aligned with the demands of next-generation intelligent transportation systems.

Bibliography

[1] U.S. Department of Transportation (USDOT), "Intelligent transportation systems (its) joint program office strategic plan 2020–2025," 2020. [Online]. Available: https://www.its.dot.gov/stratplan2020/

[2] European Commission, "Directive 2010/40/eu of the european parliament and of the council of 7 july 2010 on the framework for the deployment of intelligent transport systems in the field of road transport and for interfaces with other modes of transport," 2010.

[3] P. D. Groves, "The challenges of GNSS in urban canyons," *Inside GNSS*, vol. 8, no. 2, pp. 40–47, 2013.

[4] P. Misra and P. Enge, *Global Positioning System: Signals, Measurements, and Performance*, 2nd ed. Lincoln, MA, USA: Ganga-Jamuna Press, 2011.

[5] J. Petit and S. E. Shladover, "Potential cyberattacks on automated vehicles," *IEEE Trans. Intell. Transp. Syst.*, vol. 16, no. 2, pp. 546–556, Apr. 2015.

[6] H. Wymeersch, J. Lien, and M. Z. Win, "Cooperative localization in wireless networks," *Proc. IEEE*, vol. 97, no. 2, pp. 427–450, Feb. 2009.

[7] D. Karunatilaka, F. Zafar, V. Kalavally, and R. Parthiban, "LED based indoor visible light communications: State of the art," *IEEE Commun. Surveys Tuts.*, vol. 17, no. 3, pp. 1649–1678, 3rd Quart. 2015.

[8] A. Memedi and F. Dressler, "Vehicular visible light communication: A survey," *IEEE Commun. Surveys Tuts.*, vol. 23, no. 1, pp. 161–181, 1st Quart. 2021.

[9] J. Armstrong, "OFDM for optical communications," *J. Lightw. Technol.*, vol. 27, no. 3, pp. 189–204, Feb. 2009.

[10] A. R. Ndjiongue and H. C. Ferreira, "An overview of outdoor visible light communications," *Phys. Commun.*, vol. 27, pp. 32–46, 2018.

[11] H. Haas, L. Yin, Y. Wang, and C. Chen, "What is LiFi?" *J. Lightw. Technol.*, vol. 34, no. 6, pp. 1533–1544, Mar. 2016.

[12] Z. Ghassemlooy, W. Popoola, and S. Rajbhandari, *Optical Wireless Communications: System and Channel Modelling with MATLAB®*. Boca Raton, FL, USA: CRC Press, 2013.

[13] N. Kumar, D. Terra, and N. Lourenco, "Visible light positioning: A survey," *Wireless Pers. Commun.*, vol. 107, pp. 1065–1107, 2019.

[14] T. Komine and M. Nakagawa, "Fundamental analysis for visible-light communication system using LED lights," *IEEE Trans. Consum. Electron.*, vol. 50, no. 1, pp. 100–107, Feb. 2004.

[15] E. Hecht, *Optics*, 5th ed. Harlow, UK: Pearson Education, 2017.

[16] S. Schmid, G. Corbellini, S. Mangold, and T. R. Gross, "Retroreflective visible light communication," in *Proc. 23rd Annu. Int. Conf. Mobile Comput. Netw. (MobiCom)*, 2017, pp. 522–524.

[17] Z. Zhang, X. Zhang, and H. Liu, "Modulated retroreflective visible light communication for indoor positioning," *IEEE Photon. J.*, vol. 10, no. 2, pp. 1–15, Apr. 2018, art. no. 7902715.

[18] S. Dimitrov and H. Haas, *Principles of LED Light Communications: Towards Networked Li-Fi*. Cambridge, UK: Cambridge Univ. Press, 2015.

[19] A. L. Barrios and M. Morales-Céspedes, "Exploiting angular diversity for passive positioning VLC systems," in *Proc. IEEE ICC Workshops (WS17)*, 2025, pp. 474–479.

[20] S. Shao, A. Salustri, A. Khreishah, C. Xu, and S. Ma, "R-vlcp: Channel modeling and simulation in retroreflective visible light communication and positioning systems," *IEEE Internet of Things Journal*, vol. 10, no. 13, pp. 11 429–11 439, Jul. 2023.

[21] M. Morales-Céspedes, B. G. Guzmán, V. P. G. Jiménez, and A. G. Armada, "Aligning the light for vehicular visible light communications," *IEEE Veh. Technol. Mag.*, vol. 18, no. 1, pp. 59–69, Mar. 2023.

[22] A. L. Barrios and M. Morales-Céspedes, "On the design of wide FoV angle diversity receivers for vehicle-to-vehicle VLC," in *Proc. 2024 IEEE 99th Vehicular Technology Conference (VTC-Spring)*, 2024, pp. 1–6.

[23] A. Egidi, "Review of main optical retroreflectors," Technical Report, Tech. Rep., Nov. 2018.

[24] D. A. Arnold, "Method of calculating retroreflector-array transfer functions," Smithsonian Institution Astrophysical Observatory, Tech. Rep. SAO Special Rep. 382, Feb. 1979.

[25] M. Morales-Céspedes, H. Haas, and A. G. Armada, "Optimization of the receiving orientation angle for zero-forcing precoding in VLC," *IEEE Commun. Lett.*, vol. 25, no. 3, pp. 921–925, Mar. 2021.

[26] J. R. Barry and J. M. Kahn, "Link design for nondirected wireless infrared communications," *Appl. Opt.*, vol. 34, no. 19, pp. 3764–3776, Jul. 1995.

[27] N. Kopeika and J. Bordogna, "Background noise in optical communication systems," *Proc. IEEE*, vol. 58, no. 10, pp. 1571–1577, Oct. 1970.

[28] M. S. Islim *et al.*, "The impact of solar irradiance on visible light communications," *J. Lightw. Technol.*, vol. 36, no. 12, pp. 2376–2386, Jun. 2018.

[29] E. Eso, Z. Ghassemlooy, S. Zvanovec, J. Sathian, and A. Gholami, "Fundamental analysis of vehicular light communications and the mitigation of sunlight noise," *IEEE Trans. Veh. Technol.*, vol. 70, no. 6, pp. 5932–5943, Jun. 2021.

[30] P. Sharda and M. R. Bhatnagar, "Vehicular visible light communication system: Modeling and visualizing the critical outdoor propagation characteristics," *IEEE Trans. Veh. Technol.*, vol. 72, no. 11, pp. 14 317–14 329, Nov. 2023.

[31] S. Ma *et al.*, "Optimal power allocation for integrated visible light positioning and communication system with a single LED-lamp," *IEEE Trans. Commun.*, vol. 70, no. 10, pp. 6734–6747, Oct. 2022.